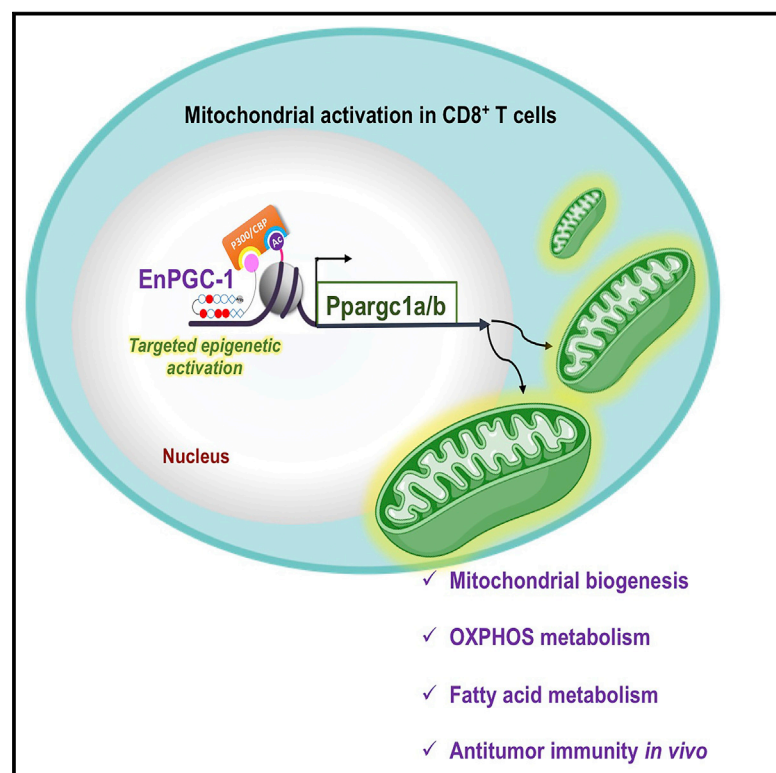


Cell Chemical Biology

Targeted epigenetic induction of mitochondrial biogenesis enhances antitumor immunity in mouse model

Graphical abstract



Authors

Madhu Malinee,
Ganesh Namasivayam Pandian,
Hiroshi Sugiyama

Correspondence

ganesh@kuchem.kyoto-u.ac.jp (G.N.P.),
hs@kuchem.kyoto-u.ac.jp (H.S.)

In brief

Malinee et al. develop a bifunctional epigenetic modulator, EnPGC-1, encompassing p300/CBP-selective bromodomain inhibitor and pyrrole-imidazole polyamides. EnPGC-1 mediates epigenetic induction of mitochondrial biogenesis in CD8⁺ T cells, skews the metabolism toward oxidative phosphorylation, and boosts antitumor effect of PD-L1 checkpoint in a mouse model.

Highlights

- A DNA-based epigenetic activator for PGC-1 α/β called EnPGC-1 is developed
- EnPGC-1 triggers the mitochondrial biogenesis in CD8⁺ T cells
- Genome and epigenome profiling suggest site-specific transcriptional activation
- EnPGC-1 synergizes PD-1 blockade and enhances the tumor inhibition in mouse model

Article

Targeted epigenetic induction of mitochondrial biogenesis enhances antitumor immunity in mouse model

Madhu Malinee,¹ Ganesh Namasivayam Pandian,^{2,*} and Hiroshi Sugiyama^{3,4,*}

¹Department of Anatomy and Developmental Biology, Graduate School of Medicine, Kyoto University, Kyoto, Japan

²Institute of Integrated Cell Material Sciences (iCeMS), Kyoto University of Advanced Study, Kyoto, Japan

³Department of Chemistry, Graduate School of Science, Kyoto University, Kyoto, Japan

⁴Lead contact

*Correspondence: ganesh@kuchem.kyoto-u.ac.jp (G.N.P.), hs@kuchem.kyoto-u.ac.jp (H.S.)

<https://doi.org/10.1016/j.chembiol.2021.08.001>

SUMMARY

Considering the potential of combinatorial therapies in overcoming existing limitations of cancer immunotherapy, there is an increasing need to identify small-molecule modulators of immune cells capable of augmenting the effect of programmed cell death protein 1 (PD-1) blockade, leading to better cancer treatment. Although epigenetic drugs showed potential in combination therapy, the lack of sequence specificity is a major concern. Here, we identify and develop a DNA-based epigenetic activator with tri-arginine vector called EnPGC-1 that can trigger the targeted induction of the peroxisome proliferator-activated receptor-gamma coactivator 1 alpha/beta (PGC-1 α/β), a regulator of mitochondrial biogenesis. EnPGC-1 enhances mitochondrial activation, energy metabolism, proliferation of CD8⁺ T cells *in vitro*, and, in particular, enhances oxidative phosphorylation, a feature of long-lived memory T cells. Genome-wide gene analysis suggests that EnPGC-1 and not the control compounds can regulate T cell activation as a major biological process. EnPGC-1 also synergizes with PD-1 blockade to enhance antitumor immunity and improved host survival.

INTRODUCTION

Cancer immunotherapy based on programmed cell death 1 (PD-1)-blockade has gained exponential interest over the last decade because of long-term clinical benefits, and effectiveness over conventional therapies. PD-1 is an immunoinhibitory receptor expressed on activated immune effector CD8⁺ T cells and regulates tolerance and immunity (Dunn et al., 2004; Fife and Bluestone, 2008). Cancer cells and other immune cells express programmed death-ligand PD-L1/PD-L2 (ligands of PD-1), and the PD-1/PD-Ls interaction leads to the inactivation of T cell functions. The blockade of PD-1/PD-Ls axis reinvigorates the T cell functions and enhances antitumor immunity (Leach et al., 1996; Iwai et al., 2002). The US Food and Drug Administration (FDA) has approved the PD-1 blockade therapy using monoclonal antibodies (mAbs) to PD-1 or its ligand PD-L1 for a wide range of cancers (Chamoto et al., 2020; Kumar and Chamoto, 2021).

Despite several advantages of PD-1 blockade therapy, the major limitation is that more than half the population of cancer patients remain unresponsive to PD-1 blockade monotherapy. Although numerous clinical trials have been performed for blocking PD-1/PD-Ls alone or in combination with other negative receptors (such as Lag3 and Tim-3) or other physicochemical therapies, the clinical outcomes reported to date are not

satisfactory. Consequently, efforts are on developing novel cost-effective combination therapies aimed at rescuing the less-responsive cancer patients.

Mitochondrial activation is known to be critical for CD8⁺ T cell activation, proliferation, and memory cell fate determination during immune responses (Weinberg et al., 2015; Buck et al., 2016, 2017; van der Windt et al., 2013; Sena et al., 2013). Recently, the Honjo group demonstrated that mitochondrial-activating chemicals improve PD-1 blockade (Chamoto et al., 2017) and revealed that reactive oxygen species (ROS) generators (e.g., dinitrophenol, Luperox) and mitochondrial uncouplers (e.g., FCCP [carbonilcyanide p-trifluoromethoxyphenylhydrazone]) could synergize the tumoricidal effect of PD-1 blockade where the cytotoxic T lymphocytes (CTLs) showed enhanced AMPK and mTOR expression in the combination group. Further, they found PGC-1 α (the downstream molecule of AMPK/mTOR) upregulated in the combination group and a series of chemical activators of this ROS-AMPK/mTOR-PGC-1 pathway synergize with PD-1 blockade and enhances antitumor immunity (Chamoto et al., 2017). PGC-1 α , and PGC-1 β , the known coactivators, form complexes with different transcription factors (TFs) and regulate the expression of genes associated with mitochondrial biogenesis, metabolism, oxidative phosphorylation (OXPHOS), fatty acid oxidation (FAO), and mitochondrial cristae reorganization (Lin et al., 2005; St-Pierre et al., 2003). Based on these

reports, enhancing mitochondrial OXPHOS and FAO in CD8⁺ T cells could be a good approach to boost antitumor immunity in combination with PD-1 blockade therapy.

Small-molecule modulators of epigenetic enzymes have shown clinical potential to enhance the efficacy of cancer immunotherapy owing to their potency to alter multi-gene networks (Zhu et al., 2016; Gallagher et al., 2017). However, the lack of sequence selectivity leading to potential side effects and toxicity has been a major road barrier in their clinical use. Therefore, artificial transcriptional control achieved by combining the epigenetic modulator with a sequence-recognizing ligand is in demand (Zhu et al., 2016; Kobayashi et al., 2021). The Dervan group first developed the small-molecular compound pyrrole-imidazole polyamide (PIP), which can recognize DNA base pairs with sequence specificity (Dervan and Edelson, 2003). An anti-parallel pairing of imidazole and pyrrole (I-P) recognizes a G:C base pair, whereas a pyrrole-pyrrole pairing (P-P) recognizes A:T or T:A. The unique properties of PIP molecules, e.g., sequence specificity, smooth permeability to the cell/nuclear membrane, and binding affinity similar to that of natural TFs, render it a promising small-molecule candidate for therapeutic usage (Takahashi et al., 2008; Hiraoka et al., 2015; Malinee et al., 2020). We harnessed the capability of sequence-specific binding of PIPs and supplemented selectivity to epigenetic modulators (e.g., suberoylanilide hydroxamic acid [SAHA], a histone deacetylase [HDAC] inhibitor, and an epigenetic eraser; and CTB [N-(4-chloro-3-trifluoromethyl-phenyl)-2-ethoxy-benzamide], a histone acetyltransferase [HAT] activator, and an epigenetic writer) by conjugating them with PIPs (Pandian et al., 2014a, 2014b; Han et al., 2015).

Here, we show the identification and development of a designer ligand conjugated with bromodomain inhibitor (BI), an epigenetic reader capable of inducing the expression of PGC-1 α/β , and termed it EnPGC-1. EnPGC-1 remarkably activated the downstream genes of PGC-1 α/β that regulate OXPHOS, FAO, and longevity of CD8⁺ T cells both *in vitro* and *in vivo*. Furthermore, the combination therapy using EnPGC-1 with PD-1 blockade notably enhanced antitumor immunity and improved the survival of tumor-bearing mice compared with PD-1 blockade or PIP-alone treatment. Our programmable DNA-based epigenetic activator could open a new avenue to treat less-responsive cancer patients in combination with PD-1 blockade.

RESULTS

Design of epigenetically active PIP (EnPGC-1) for PGC-1 α/β activation

Considering the clinical importance of modulating PGC-1 expression, we screened our databank generated from a library of SAHA-conjugated PIPs on human dermal fibroblast (HDF) cells for a specific PIP sequence that upregulates the mitochondrial-biogenesis-associated gene network. While analyzing the microarray results of a library of 32 SAHA-PIPs (Pandian et al., 2014b), we discovered a PIP named SAHA-PIP R that specifically activated the endogenous expression of PGC-1 α (encoded by PPARGC1A gene) and PGC-1 β (encoded by PPARGC1B gene) in HDF cells (Figure S1A). This preliminary finding suggests that the PIP sequence R may have the specificity toward gene PPARGC1A/B (Figures 1A and S1G). We verified the microarray

data by treating HDF cells with SAHA-R for 48 h and quantified the transcript level of PGC-1 α/β (Figures S1B and S1C). We also confirmed the target specificity of the sequence R toward the activation of PGC-1 α/β using HAT activator (CTB)-conjugated PIP R (Figure S1C). However, the epigenetic modifiers SAHA and CTB are indirect approaches to gene activation that solely depend on the presence of the HAT enzyme in the gene vicinity. To improve gene activation, we hypothesized that the recruitment of epigenetic activators for histone acetylation could be a more direct and improved way to activate a gene of interest compared with the blockage of the epigenetic suppressor. Recently, our research group developed a novel epigenetic modulator for locus-specific acetylation that can directly recruit the acetylation machinery (P300/CBP) in the PIP-binding region. This epigenetic reader (BI) recognizes the bromodomain (BD) of the p300 protein (Taniguchi et al., 2018). Furthermore, the HAT domain of p300 facilitates sequence-specific acetylation in the PIP-binding region. To harness the benefit of this strategy, we conjugated PIP sequence R with BI and tested the effect of BIR on HDF cells (Figure S1H). Compared with SAHA-R and CTB-R, BIR yields a better enhancement in the expression of PGC-1 α as well as PGC-1 β (Figures S1B and S1C). Notably, the control molecules “R alone” and “BI alone” did not enhance the PGC-1 α/β transcript levels, as per our expectation, because BI alone does not have sequence specificity, and R alone, although it has sequence specificity, lacks functional epigenetic activity; however, their combination (i.e., BIR) had both sequence specificity as well as functional epigenetic activity (Figure S1C). This implies that, specifically, cognate sequence of R is directly or indirectly involved in the upregulation of PGC-1 α/β .

In a further development, we added three arginine repeats at the C terminus of BIR, which eases the uptake of PIPs in the cell (Hidaka et al., 2020). We named this designer ligand BiR-Arg3 (BIR with three arginine repeats) EnPGC-1. The structure of EnPGC-1 is shown in Figure 1A (also see Figure S1I). The expression of PGC-1 α/β at the transcript level was enhanced in HDF cells treated with EnPGC-1 in a dose-dependent manner compared with the DMSO vehicle treatment (Figure S1D).

Recent work suggests that enhancing OXPHOS in CD8⁺ T cells boosts the longevity of T cells and improves antitumor immunity (Chamoto et al., 2017), and the effector T cells are known to become less active in the suppressive tumor microenvironment because of reduced PGC-1 expression (Scharping et al., 2016). PGC-1 α and PGC-1 β possess homology and have a similar gene regulation pattern (Lin et al., 2002; Kressler et al., 2002). Since these coactivators share common structural features in the protein structure in human and mice, we were curious to examine whether EnPGC-1 could enhance PGC-1 α/β expression in mouse primary CD8⁺ T cells *in vitro*. Following the schedule mentioned in Figure 1B, we quantified the transcript level of PGC-1 α/β in CD8⁺ T cells and found that EnPGC-1 affords a better enhancement of the expression of PGC-1 α and PGC-1 β compared with BIR (Figure 1C). Further, the transcript levels of PGC-1 α/β were enhanced significantly ($p < 0.05$) in a dose-dependent manner by EnPGC-1 treatment compared with DMSO and control conjugated mismatch PIP (BI_{Ctrl}-Arg3, control PIP hereafter) (Figure 1D). Control PIP has a similar chemical architecture to EnPGC-1 but has different sequence

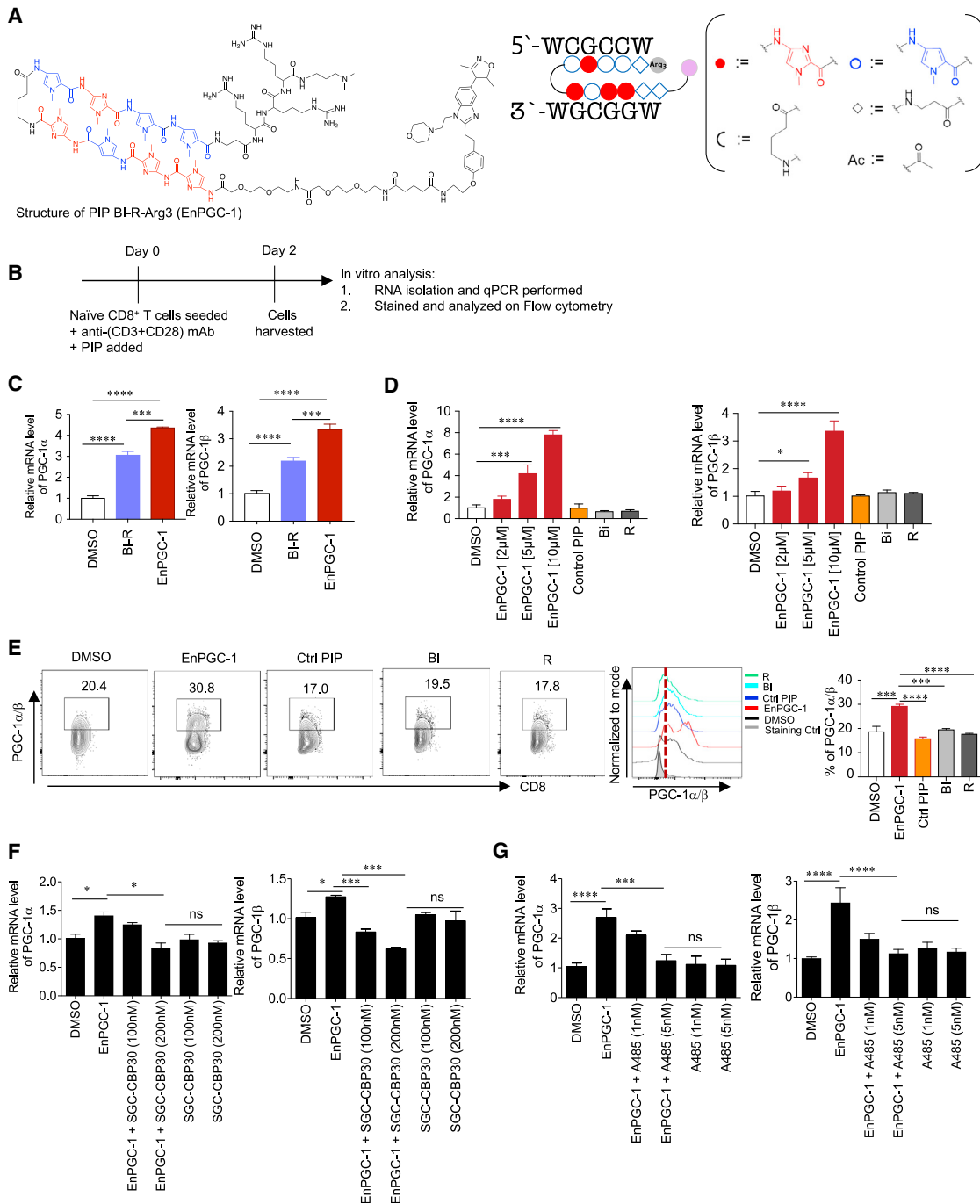


Figure 1. Synthetic sequence-specific epigenetic modulator, EnPGC-1, enhances PGC-1 α/β expression

(A) Structural design of EnPGC-1.

(B) Schematic representation of experimental schedule for (C) to (G).

(C and D) Transcript levels of PGC-1 α (left) and PGC-1 β (right) in CD8⁺ T cells treated with 5 μ M or indicated concentration of EnPGC-1, BIR, BI, and R.

(E) PGC-1 α/β protein level was quantified using flow cytometry. Representative fluorescence-activated cell sorting (FACS) pattern (left), histogram (middle), and bar graph showing frequency of PGC-1 α/β (right).

(F) Transcript level of PGC-1 α (left) or PGC-1 β (right) in CD8⁺ T cells treated with EnPGC-1 and SGC-CBP30 (100 nM and 200 nM).

(G) Transcript level of PGC-1 α (left) or PGC-1 β (right) in CD8⁺ T cells treated with EnPGC-1 and A485 (1 nM and 5 nM).

(C–G) One-way ANOVA analysis. * $p < 0.05$, ** $p < 0.01$, *** $p < 0.001$, **** $p < 0.0001$, means \pm SEM, $n = 3$ wells. Data are representative of three independent experiments.

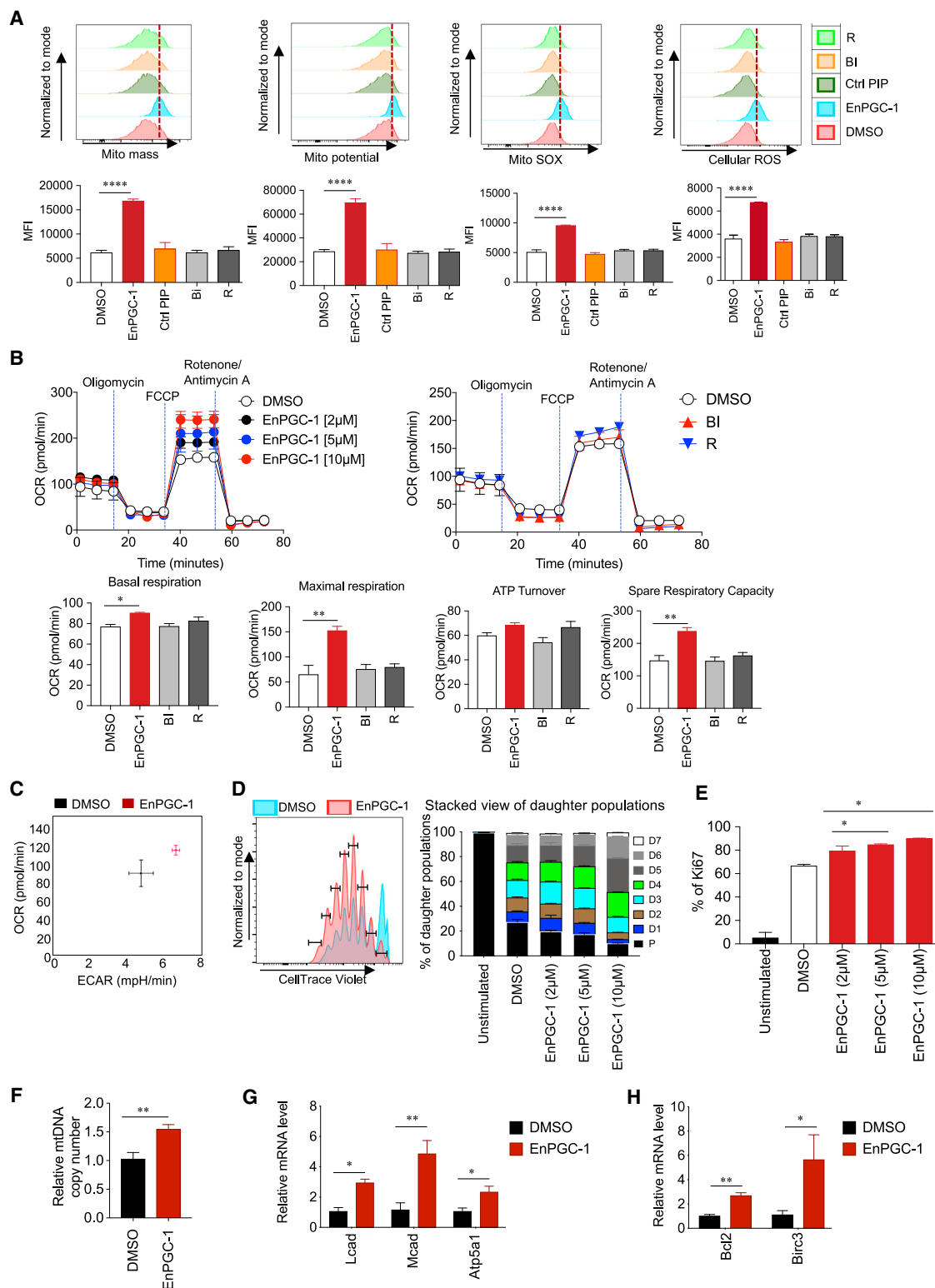


Figure 2. EnPGC-1 enhances mitochondrial activation, proliferation, and mitochondrial biogenesis in CD8⁺ T cells *in vitro*

Following the schedule in Figure 1B, all *in vitro* analyses were performed post 48 h of treatment except (D)–(E) where cells were analyzed at 72 h.

(A) Mitochondrial activation parameters (mitochondrial mass, potential, mitoSox, and cellular ROS) were assessed using mitochondrial dyes. Representative histogram (upper) and mean fluorescence intensity (MFI) of different mito dyes (lower) are shown.

(legend continued on next page)

recognition (Figure S1J). Further, we quantified the expression of PGC-1 α/β at the protein level by staining intranuclearly in treated CD8⁺ T cells using flow cytometry. EnPGC-1 notably enhanced the expression of PGC-1 α/β while the control PIPs did not (Figure 1E).

Together, these results suggest that EnPGC-1 enhances the expression of PGC-1 α/β while the control PIP with similar architecture but different sequence recognition does not show PGC-1 α/β enhancement. Notably, EnPGC-1 (arginine-conjugated BIR) yields improved enhancement in the expression of PGC-1 α/β compared with other epigenetic activator conjugated PIP (e.g., SAHA-R/CTB-R) and BIR. The control BI alone and PIP R alone, which lack sequence specificity and epigenetic activity, respectively, have no effect.

We hypothesize that EnPGC-1, a bifunctional molecule, functions via binding to p300's bromodomain and recruiting it to PIP-binding region, causing acetylation and gene expression. To test our hypothesis, we performed a squelching assay, where we used SGC-CBP30, a potent CREBBP/EP300 (CBP/p300) inhibitor, to test whether co-administration of free SGC-CBP30 cancels the gene enhancement effect of EnPGC-1. We treated murine primary CD8⁺ T cells following the schedule mentioned in Figure 1B. We found that the co-administration of SGC-CBP30 significantly ($p < 0.05$) reduces the gene expression level of PGC-1 α/β compared with EnPGC-1 alone (Figures 1F and S1E). Further, we tested the involvement of acetyltransferase activity of p300 for EnPGC-1-mediated gene induction. We co-administered A-485, a potent p300 acetyltransferase inhibitor to CD8⁺ T cell culture along with EnPGC-1. The co-administration of A-485 abrogates the effect of EnPGC-1. The co-administration of A-485 significantly ($p < 0.001$) reduces the gene expression level compared with treatment with EnPGC-1 alone, which further strengthens the mechanism of action of bifunctional EnPGC-1 for enhancing the PGC-1 gene expression (Figures 1G and S1F). Together, these two results suggest that EnPGC-1 functions as a bifunctional recruiter and induces HAT activity of p300.

EnPGC-1 enhances mitochondrial function and proliferation in murine CD8⁺ T cells *in vitro*

As PGC-1 is the master regulator of mitochondrial activation and biogenesis, we assessed mitochondrial activation parameters in murine primary CD8⁺ T cells treated with EnPGC-1 as per the schedule in Figure 1B. We found that EnPGC-1 and not control PIP enhanced mitochondrial activation parameters (mitochondrial mass, potential, mitochondrial superoxide [MSOX], and cellular ROS [CROX]) in CD8⁺ T cells (Figure 2A). Further, using Seahorse flux analyzer, we measured both mitochondrial respi-

ration (denoted by the oxygen consumption rate [OCR]) and glycolytic respiration (denoted by the extracellular acidification rate [ECAR]) (Figure S2A). EnPGC-1 treatment shows enhancement in OCR dose dependently in CD8⁺ T cells (Figure 2B, upper). Further, OCR-associated parameters, such as basal respiration, maximal respiration, and ATP turnover, were higher in the EnPGC-1-treated condition over DMSO vehicle, while the controls (i.e., BI alone and R alone) did not show any enhancement (Figure 2B, lower). Notably, spare respiratory capacity (SRC), which is linked to cell survival, was significantly ($p < 0.01$) higher in the EnPGC-1-treated group over DMSO vehicle and other controls (Figure 2B, lower panel). Enhancement of SRC by EnPGC-1 treatment suggests that CD8⁺ T cells can survive longer (van der Windt et al., 2012). A similar enhancement in OCR was observed dose dependently in HDF cells (Figure S2B).

It is reported that cardiomyocytes express both PGC-1 α and PGC-1 β (Lin et al., 2002; Puigserver et al., 1998); thus, we tested the effect of EnPGC-1 and measured the OCR, which we confirmed was enhanced compared with the DMSO vehicle treatment (Figure S2C).

In addition, we measured glycolytic respiration and found that EnPGC-1 treatment enhanced it minimally in CD8⁺ T cells (Figure S2D). Furthermore, we calculated the ratio of basal OCR/basal ECAR in treated CD8⁺ T cells, suggesting the selective dependency of cells regarding their energy demand (Figure 2C). The higher OCR/ECAR value observed in the EnPGC-1-treated condition suggests that EnPGC-1 treatment skews the CD8⁺ T cell metabolism toward more OXPHOS (Figure 2C). Increased mitochondrial activation parameters and OCR together indicate that the induced expression of PGC-1 α/β by EnPGC-1 treatment results in skewed metabolism toward OXPHOS.

T cell receptor (TCR) stimulation in naive CD8⁺ T cells triggers a plethora of signaling networks. During priming, T cells depend primarily upon glycolysis for their bioenergetic needs and anabolic profile (van der Windt and Pearce, 2012; Pearce, 2010). We tested whether the enforced PGC-1 α/β expression and mitochondrial enhancement during TCR stimulation have any positive effect on the early phase of CD8⁺ T cell differentiation and proliferation; we assessed the proliferation of CD8⁺ T cells using the dye dilution method and compared the rate of proliferation among the treated groups. The frequency of daughter populations was plotted in a stacked graph (Figure 2D). Interestingly, we found that EnPGC-1 treatment enhanced the proliferation of CD8⁺ T cells in a dose-dependent manner (Figure 2D). Proliferation assessment using Ki67 (a proliferation marker) gives a similar result (Figure 2E). Based on this result, we conclude that enhancing mitochondrial activation by

(B) OCR of CD8⁺ T cells treated with EnPGC-1 (2, 5, 10 μ M) and controls (BI and R, each 5 μ M) are shown (upper). OCR-associated parameters were calculated and compared among treated groups (5 μ M each) (lower).

(C) The double plot of OCR/ECAR was plotted (using measurement before oligomycin injection).

(D and E) Proliferation was assessed 72 h post stimulation of CellTrace Violet (CTV)-labeled naive CD8⁺ T cells treated with EnPGC-1 by dye dilution method (D) or by Ki67 (a proliferation marker) staining method (E). (D) Histogram of dye dilution for DMSO and EnPGC-1 (5 μ M) treatment (left). The undivided population (high CTV intensity) is the parent population (denoted as P). Different daughter populations (namely D1–D7) were compared in stacked view (right). (E) From the experimental groups of Figure 2D, cells were stained with Ki67 and frequency of Ki67 is shown.

(F) mtDNA copy number (mt-ND1/nu-HK2) was assessed in CD8⁺ T cells.

(G and H) Transcript level of different genes were assessed by qRT-PCR from the naive CD8⁺ T cells treated with EnPGC-1 (5 μ M).

(A, B, D, E, G, and H) Means \pm SEM, $n = 3$ wells, * $p < 0.05$, ** $p < 0.01$, *** $p < 0.001$, **** $p < 0.0001$, one-way ANOVA analysis. (F) Means \pm SEM, $n = 3$ wells. ** $p < 0.01$, two-tailed student t test analysis. Data are representative of three independent experiments.

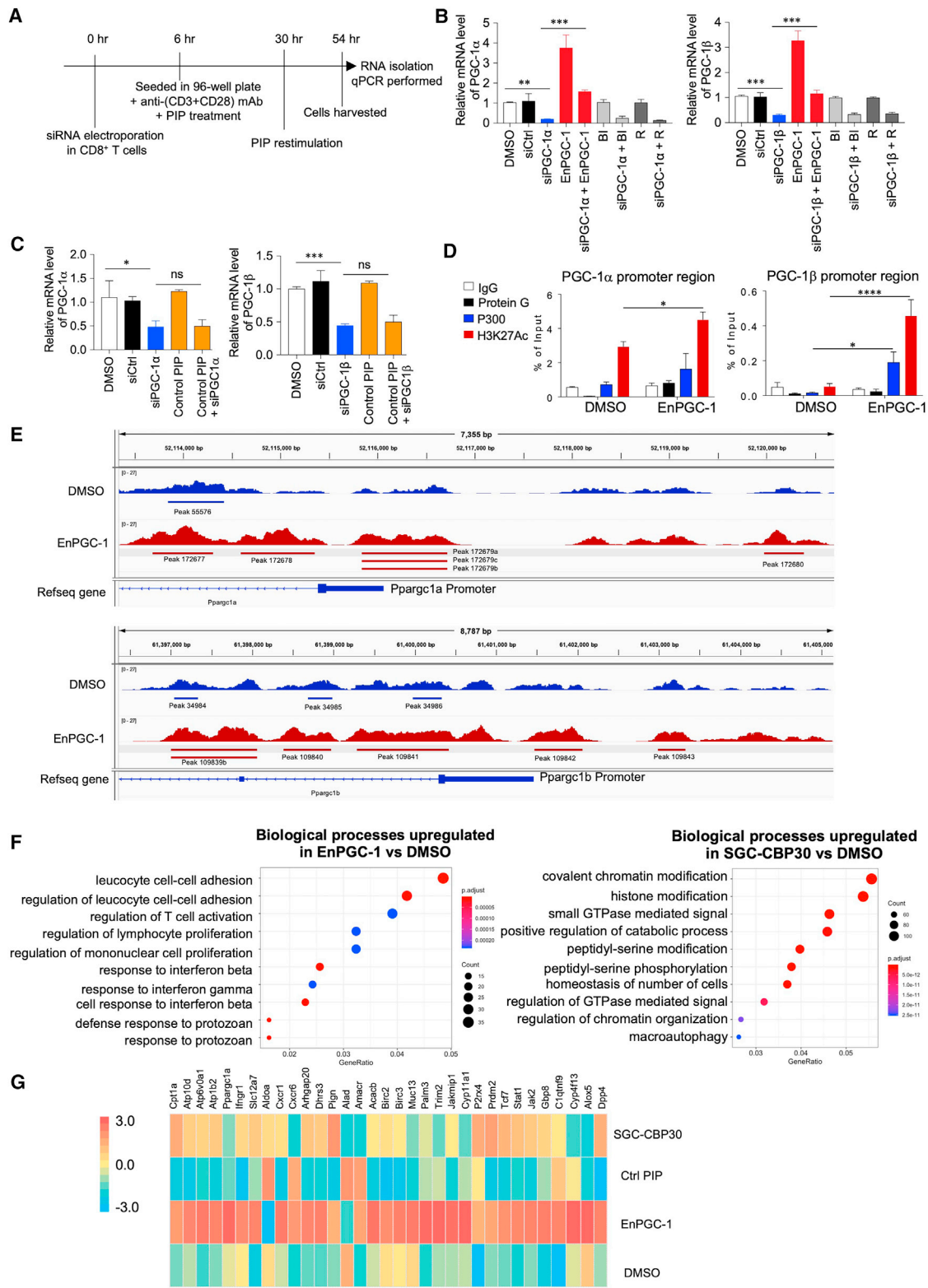


Figure 3. EnPGC-1 recruit the acetylation machinery and promote locus-specific acetylation in promoter region and enhance transcription of PGC- α/β

(A) Schematic representation of experimental schedule of siRNA-mediated knockdown assay.

(B and C) Transcript level of PGC-1 α (left) or PGC-1 β (right) in CD8 $^+$ T cells from indicated treated groups of siRNA assay.

(legend continued on next page)

EnPGC-1 treatment positively regulates T cell differentiation at the early phase.

The coactivators PGC-1 α/β are inducers of mitochondrial biogenesis and respiration and they modulate the composition and function of individual mitochondria (Lin et al., 2002). Curiously, we assessed mitochondrial DNA (mtDNA) copy number (mt-ND1/nu-HK2). The result suggests that EnPGC-1-induced PGC-1 α/β upregulation increased mtDNA copy number, suggestive of enhanced mitochondrial biogenesis in CD8⁺ T cells (Figure 2F).

PGC-1 α/β is a known transcriptional coactivator that controls global oxidative metabolism (OXPHOS, FAO) by establishing complexes with TFs; e.g., PPAR, NRF, and ERR (Villena and Kralli, 2008). Acyl-coenzyme A (CoA) dehydrogenase long chain (LCAD), and acyl-CoA dehydrogenase medium chain (MCAD) are important enzymes associated with FAO, which were found upregulated in the EnPGC-1-treated group (Figure 2G). Since EnPGC-1 treatment enhances OXPHOS, we quantified transcript level of ATP synthase F1 subunit alpha (ATP5a1), a subunit of ATP synthase enzyme that catalyzes ATP synthesis using an electrochemical gradient of protons across the inner membrane during OXPHOS. The transcript level of ATP5a1 was higher in the EnPGC-1-treated group than in the DMSO-treated group (Figure 2G). The expression level of ATP5a1 is in line with our phenotypic observation (enhanced OCR) (Figure 2B).

Since enhanced OXPHOS and FAO improves the longevity of cells, we quantified the transcript level of anti-apoptotic genes Bcl2 and Birc3 in the *in vitro* stimulated CD8⁺ T cells treated with EnPGC-1 (van der Windt et al., 2012; Chowdhury et al., 2018). EnPGC-1-treated CD8⁺ T cells show higher expression level of Bcl2 and Birc3 (Figure 2H).

Taken together, EnPGC-1 contributed to an increase in oxidative metabolism by enhancing mitochondrial respiration (OXPHOS and FAO), and mitochondrial biogenesis (mtDNA copy number). Importantly, this elevated oxidative metabolism by EnPGC-1 results in enhanced T cell differentiation to effector population at an early phase with enhanced longevity.

EnPGC-1 triggers sequence-specific activation of PGC-1 α/β expression through targeted acetylation

To address the specificity of EnPGC-1 for the activation of PGC-1 α/β expression, we used a small interfering RNA (siRNA)-mediated knockdown assay to test whether EnPGC-1 can rescue the gene expression. We transfected naive CD8⁺ T cells with a siRNA against the transcript of PGC-1 α and treated with or without EnPGC-1 along with TCR stimulation (Figure 3A). Treatment with the siRNA against PGC-1 α reduced the level of PGC-1 α transcript ($p = 0.0047$). The enhanced expression of PGC-1 α by EnPGC-1 treatment rescued the effect of siRNA when administered together with the siRNA (Figure 3B). A similar result was

obtained for the siRNA-mediated knockdown of PGC-1 β expression, suggesting the direct effect of EnPGC-1 in the activation of PGC-1 α and PGC-1 β at the transcript level (Figure 3B; Figure S3A). Furthermore, the controls (BI alone, R alone, and control PIP) did not rescue the siRNA effect (Figures 3B and 3C).

To examine the binding affinity and sequence selectivity of EnPGC-1, a DNA melting temperature (T_m) assay was performed (Vaijayanthi et al., 2012). T_m assay allows the measurement of relative binding affinities through the T_m and ΔT_m values ($\Delta T_m = T_m(\text{DNA} + \text{PIP}) - T_m(\text{DNA})$). To confirm the binding, dsDNA templates were prepared, e.g., a matched DNA template (5'-GGCACGCCTCGG-3' [EnPGC1-DNA], and a mismatched DNA template with a different sequence, 5'-GGCAGACGTC GG-3' [mismatch DNA]; the binding sites are underlined). The result of the T_m assay confirmed the binding of EnPGC-1 to the target DNA as a T_m shift of 19.99°C was observed, while the T_m shift was only 1.85°C for mismatch control DNA (Figure S3B). The low ΔT_m shift recorded for the mismatch DNA in the presence of EnPGC-1 indicates a lower affinity of EnPGC-1 for sequences other than the target DNA.

Histone acetylation is a primary transcription activation marker for opening up the chromatin and “switching on” the gene expression (Turner, 1991; Verdone et al., 2006). Based on the design of bifunctional compound EnPGC-1, in which the ‘BI’ component is meant to recruit the acetylation machinery of p300/CBP, we performed chromatin immunoprecipitation (ChIP) assay of p300 in murine CD8⁺ T cells treated with EnPGC-1 for 48 h. A sequence of ~200 bp from the transcription start site (TSS) in Ppargc1a and Ppargc1b promoter region was used to test the enrichment of p300 binding. As shown in Figure 3D, a significant ($p < 0.05$) enrichment of p300 binding in the promoter region of both PGC-1 α and PGC-1 β was observed. A similar result was obtained for B16 (murine melanoma) cells where p300 and H4-pan acetylation were significantly ($p < 0.05$) enriched in EnPGC-1-treated group compared with DMSO vehicle or control BI and R (Figures S3C–S3E).

Furthermore, we examined the genome-wide H3K27Ac acetylation induced by EnPGC-1 in murine CD8⁺ T cells. The qPCR of H3K27Ac-ChIP suggested a significant ($p < 0.05$) enrichment in the promoter region of both PGC-1 α and PGC-1 β (Figure 3D). ChIP-seq analysis revealed a notable peak enrichment near TSS in the promoter region of PGC-1 α and PGC-1 β in CD8⁺ T cells treated with EnPGC-1 over DMSO vehicle (GEO: GSE175849) (Figure 3E). It is important to note here that two potential binding sites of EnPGC-1 were observed in the promoter region of PGC-1 α/β where H3K27 was significantly enriched (Figure S3F).

We then performed RNA sequencing (RNA-seq) to verify if EnPGC-1 induces unique gene expression profile compared with SGC-CBP30 and control PIP (having similar chemical

(D) ChIP-PCR of p300 binding and histone H3K27 acetylation in the promoter region of PGC-1 α/β in CD8⁺ T cells treated with EnPGC-1. The amount of promoter sequence of PGC-1 α (left) and PGC-1 β (right) in the coprecipitated DNAs was determined by qRT-PCR.

(E) ChIP-seq analysis of H3K27 acetylation in promoter region of Ppargc1a (upper) and Ppargc1b (lower).

(F) RNA-seq of CD8⁺ T cells treated with PIPs (see STAR Methods). Biological processes upregulated in EnPGC-1 over DMSO (left), and SGC-CBP30 over DMSO (right).

(G) Heatmaps were generated for some particular genes related with OXPHOS, fatty acid metabolism, and T cell activation.

(B–D) Means \pm SEM, $n = 6$ wells, * $p < 0.05$, ** $p < 0.01$, *** $p < 0.001$, **** $p < 0.0001$, one-way ANOVA analysis. Data are representative of three independent experiments.

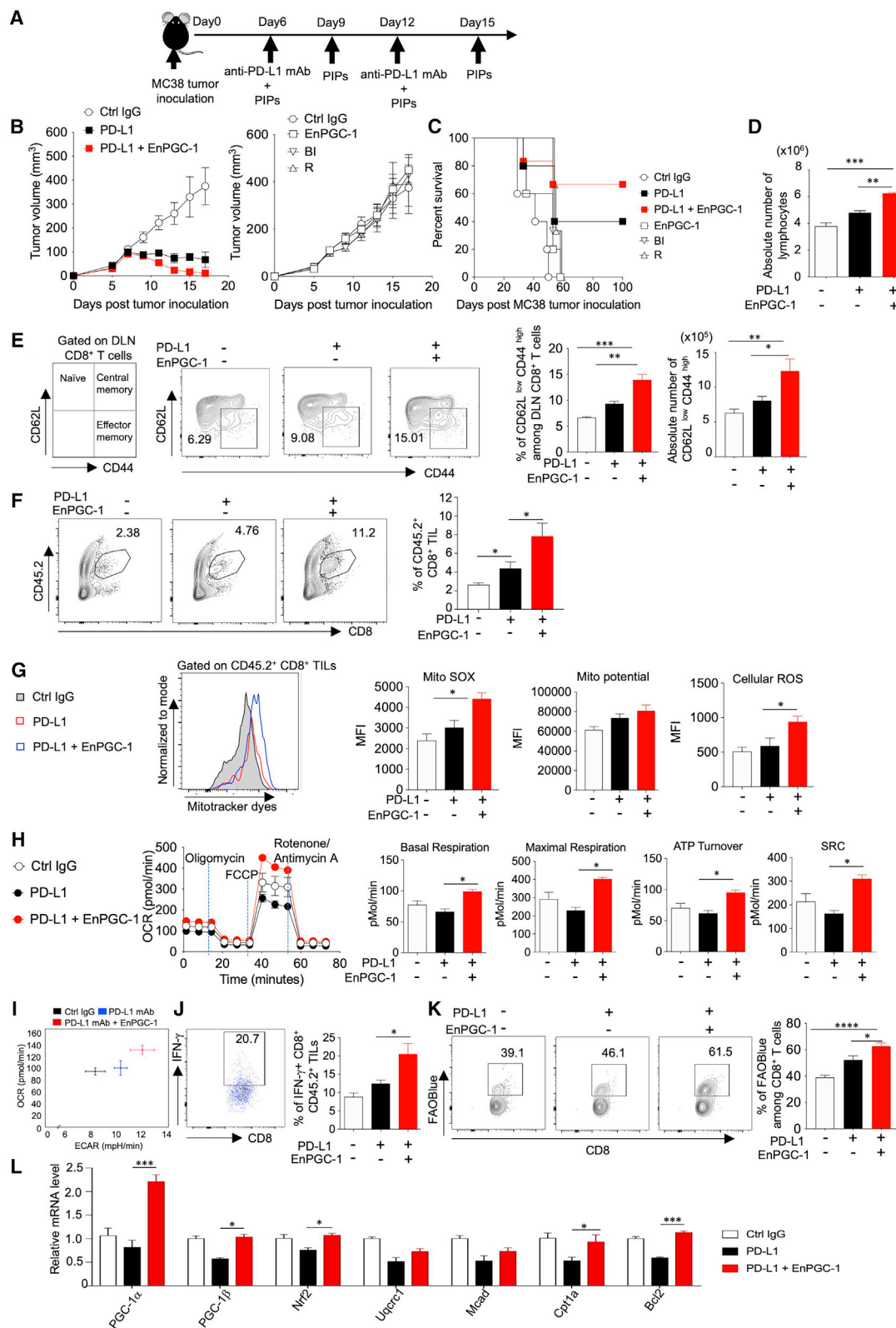


Figure 4. EnPGC-1 synergizes with PD-1 blockade therapy and improves the efficacy *in vivo*

(A) Schematic representation of *in vivo* experimental plan.

(B and C) Tumor graphs (B) and survival curve (C) were plotted (D–L). Using the experimental schedule mentioned in Figure 4A, mice were sacrificed 1 day after third treatment of PIPs (i.e., day 13) and analyzed further.

(legend continued on next page)

architecture but different recognition site) (GEO: GSE174750). RNA-seq analysis of *in vitro*-treated murine primary CD8⁺ T cells revealed that 2,308 genes ($p < 0.05$) were differentially expressed in EnPGC-1-treated cells over DMSO where 871 genes were upregulated, and 1,437 genes were downregulated (Figure S3G).

Gene Ontology (GO) analysis with differentially expressed genes (p value < 0.05) suggested that EnPGC-1 can activate immune response associated pathways as the major biological processes that included T cell activation, lymphocyte proliferation, interferon-gamma (IFN- γ) signaling, and leukocyte cell-cell adhesion (Figure 3F (left), Table S2). On the other hand, SGC-CBP30-treated cells did not show the immune-response-associated pathways but showed an entirely different set of genes (Figure 3F, right). The biological processes in the control PIP-treated cells were unrelated to immune-response-associated pathways, which further verified the site-specific gene activation in the genome-wide gene level (Figures 3G and S3H).

A heatmap of EnPGC-1-activated genes plotted along with the controls showed that the genes associated with T cell activation and maturation (Dpp4 and Tcf7) (Shao et al., 2020) and the IFN- γ signaling process (Stat1, Jak2, and Gbp7/8) (Schroder et al., 2004) were notably activated by EnPGC-1 compared with that with controls (Figure 3G). PGC-1 α signaling modulates T cell differentiation through fatty acid and OXPHOS metabolism (Choi and Bothwell, 2012). RNA-seq analysis showed that EnPGC-1 upregulated PGC-1 α (by 3.6-fold). Further, the genes related to fatty acid metabolism, like Slc12a7 (fatty acid transporter) and Cpt1a (a rate-limiting enzyme for FAO), were enhanced, which suggests that EnPGC-1 mediates FAO. Importantly, Aldoa, a gene involved in glucose metabolism, is decreased in EnPGC-1-treated cells. Also, the genes associated with the electron transport chain (OXPHOS) (e.g., Atp10d, Atp1b2) were upregulated in EnPGC-1-treated cells (Figure 3G). The enhanced transcript level of Lcad, Mcad, and Atp5a1 in the *in vitro*-stimulated and EnPGC-1-treated CD8⁺ T cells, as shown in Figure 2G, further supports that EnPGC-1 could enhance OXPHOS and FAO. Together, our results support the hypothesis that EnPGC-1-mediated induction of PGC-1 skews the metabolism toward OXPHOS/FAO.

EnPGC-1 in combination with PD-1 blockade enhances antitumor immunity

Encouraged by our *in vitro* findings that EnPGC-1 enhances PGC-1 α / β -mediated mitochondrial metabolism, OXPHOS,

FAO, and longevity in murine CD8⁺ T cells, we wondered whether EnPGC-1 could improve the effect of PD-1 blockade and enhance the antitumor immunity *in vivo*. To test our hypothesis, we performed a combination therapy on MC38 (colon adenocarcinoma, responsive tumor; Juneja et al., 2017) tumor-bearing mice using EnPGC-1 (1 mg/kg) and PD-1 blockade (using anti-PD-L1 mAb) (Figure 4A) (Kumar et al., 2020). EnPGC-1 in combination with PD-1 blockade yielded better tumor regression as well as improved survival compared with PD-1 blockade alone (Figures 4B and 4C). EnPGC-1 alone or the control molecules BI and R alone have no tumor regression effect and were not able to enhance the survival of tumor-bearing host (Figures 4B and 4C). The *in vivo* result indicates EnPGC-1 synergizes with PD-1 blockade therapy and enhances antitumor immunity.

Further, to understand how EnPGC-1 and PD-1 blockade combination ameliorates the antitumor immunity, we analyzed the experimental groups 1 day after the third treatment of EnPGC-1 *in vivo* following the schedule shown in Figure 4A. CD8⁺ T cells from draining lymph nodes (DLNs) and tumor mass were analyzed. The absolute number of DLN cells (total DLN cells per DLN) was higher in the combination group compared to anti-PD-L1 mAb alone (Figure 4D). Since the effector memory (CD62L^{low} CD44^{high}) CD8⁺ T cells in DLN are destined to leave the periphery and infiltrate the tumor mass, we compared the effector memory population among different groups and found that the frequency and the absolute number of effector memory cells were increased in the EnPGC-1 combination group significantly ($p < 0.05$) compared with PD-1 blockade alone (Figure 4E).

As CD8⁺ TILs are the real effectors to kill tumor cells and the higher frequency of infiltrated CD8⁺ T cells is the prognostic marker of immune responses, we assessed CD8⁺ TILs in the tumor mass (Idos et al., 2020). The result suggests that the frequency of infiltrated CD8⁺ T lymphocytes was higher in the combination group (Figures 4F and S4A). Further, CD8⁺ TILs from the EnPGC-1 combination group show higher mitochondrial potential, mSOX, and cellular ROS than control IgG and anti-PD-L1 mAb alone group (Figure 4G). Similar mitochondrial activation was observed in DLN CD8⁺ T cells in EnPGC-1 combination group (Figure S4B). In addition, we measured OCR to assess OXPHOS in CD8⁺ T cells (purified from pooled DLN cells). The EnPGC-1 combination exhibited significantly ($p < 0.05$) higher OCR values and its associated parameters than PD-1 blockade alone (Figure 4H). Interestingly, SRC was remarkably enhanced in combination treatment, which could result in improved

(D) Absolute number of lymphocytes (number of lymphocytes per tDLN) was calculated.

(E) Schematic representation of different population of DLN CD8⁺ T cell subsets based on the expression of CD62L and CD44 (left). Representative FACS patterns (middle) of effector memory population of tDLN CD8⁺ T cells were compared among treated groups in both frequency and absolute number (right).

(F and G) Tumor mass was harvested, homogenized using collagenase treatment, and made single-cell suspension for analysis. Tumor mass cells were stained with anti-CD8, anti-CD45.2 mAb along with mitochondrial dyes to assess mitochondrial activation. (F) Representative FACS pattern (left) of CD8⁺ TILs (CD45.2⁺ CD8⁺ T cells) and frequency (right) are shown. (G) Representative histogram of mitochondrial dye (left) and bar graph of MFI of different dyes (right).

(H) Purified CD8⁺ T cells from pooled DLN cells (of respective groups) were subjected to OCR measurement (see STAR Methods). OCR graph (left) and OCR-associated parameters (right).

(I) Double plot of OCR versus ECAR was plotted (using measurement before oligomycin injection).

(J) Representative FACS pattern of IFN- γ staining (left) and frequency of IFN- γ ⁺CD8⁺ TILs (right).

(K) Representative FACS pattern of FAOBlue staining (left) and their frequency (right) in DLN cells.

(L) Transcript level of different genes in DLN CD8⁺ T cells from *in vivo* experimental groups.

(D–H, J–K) Mean \pm SEM, $n = 5$ mice. (I, L) Means \pm SEM, $n = 3$ wells, * $p < 0.05$, ** $p < 0.01$, *** $p < 0.001$, **** $p < 0.0001$, one-way ANOVA analysis. Data are representative of three independent experiments.

longevity of effector populations *in vivo* (Figure 4H). This result is in line with our *in vitro* finding where EnPGC-1 enhances SRC of CD8⁺ T cells (Figure 2B). We also measured glycolytic respiration of DLN CD8⁺ T cells (Figure S4C). Since PD-1 blockade augments the proliferation of short-lived effector CD8⁺ T cells with glycolytic respiration, the less availability of effector T cells because of apoptotic death could be one of the possible reasons for less responsiveness in some patients (Patsoukis et al., 2015). To understand the dependency of T cells on OXPHOS/glycolysis, we plotted OCR/ECAR values and observed slightly higher glycolytic respiration (shown by ECAR) under PD-1-blockade-alone condition (Figure 4I). The combination of PD-1 blockade with EnPGC-1 (PGC-1 α/β activator) shifts the T cell dependency toward more OXPHOS than ECAR for the energy demand. This suggests skewing T cell energy metabolism toward OXPHOS enhances the effect of PD-1 blockade, which we observed in the combination group. Our result is consistent with other research groups where they have shown the drugs that enhance mitochondrial respiration improve PD-1 blockade effect (Chowdhury et al., 2018; Wan et al., 2020).

To assess the effector function, we quantified IFN- γ intracellularly in CD8⁺ TILs. The IFN- γ ⁺ CD8⁺ TILs were higher in frequency in the combination group than PD-1 blockade alone (Figure 4J).

PGC-1 family coactivators upregulate the OXPHOS and FAO metabolism (Villena and Kralli, 2008). We curiously measured the FAO in DLN CD8⁺ T cells from *in vivo* experimental animals. CD8⁺ T cells from the combination group showed higher expression of FAO compared with PD-1 blockade alone or control IgG treatment (Figure 4K). Induction of FAO in the combination group again supports the improved life of effector T cells in combating the tumor cells and enhancing antitumor immunity (Chowdhury et al., 2018; Wan et al., 2020). We further quantified the transcript level of genes associated with FAO in the purified DLN CD8⁺ T cells from *in vivo*-treated groups (1 day after third treatment of EnPGC-1) and found higher transcript levels of MCAD and Cpt1a in the combination group compared with PD-1 blockade alone (Figure 4L). Further, the transcript levels of PGC-1 α/β , Uqcrc1, and Nrf2 were also increased in the combination group (Figure 4L). The enhanced OXPHOS and FAO in the combination group improves the longevity of T cells, as indicated by elevated transcript level of Bcl2 (Figure 4L) (Paumen et al., 1997). Genes associated with mitochondrial biogenesis, like Mitofusin 1 (Mfn1, mediates mitochondrial clustering) and mitochondrial transcription factor A (TFAM, plays a role in organizing and compacting mitochondrial DNA) have shown a trend of increment in combination compared with PD-1 blockade alone (Figure S4D) (Picca and Lezza, 2015).

To conclude, the compound EnPGC-1 upregulates OXPHOS and FAO in CD8⁺ T cells, which improves the longevity and effector functions of killer T cells and augments the efficacy of PD-1 blockade in combination.

DISCUSSION

Although PD-1 blockade therapy surpassed the standard methods of cancer treatment (Topalian et al., 2015; Couzin-Frankel, 2013), unresponsiveness in a significant fraction of patients is the major limitation that needs attention (Zou et al.,

2016). The paucity of effector cells (because PD-1 blockade induced glycolysis performing effector T cells undergo apoptotic death; Patsoukis et al., 2015) at tumor sites could be one of the reasons for the unresponsiveness observed in some patients (Azimi et al., 2012; Mahmoud et al., 2011). Other research groups have emphasized the importance of inducing OXPHOS and FAO for enhancing antitumor immunity, as they generate long-lived T cells (Chowdhury et al., 2018).

In the current work, we skewed the CD8⁺ T cell metabolism toward OXPHOS and FAO by upregulating PGC-1 α and PGC-1 β , using a dual-functional molecule, EnPGC-1, encompassing the P300/CBP-selective bromodomain inhibitor (BI), which acts as a P300/CBP recruiter. Further, EnPGC-1-mediated PGC-1 α/β upregulation enhanced antitumor immunity via increased tumor-infiltrating CD8⁺ T cell frequency with enhanced mitochondrial function, OXPHOS/FAO metabolism, effector functions, and Bcl2 level *in vivo*. FAO is known for memory-like cell generation with enhanced Bcl2 level (Pearce et al., 2009; Paumen et al., 1997; Perianayagam et al., 2006). SRC enhancement in CTLs by EnPGC-1-mediated PGC-1 α/β upregulation suggests that CTLs can survive longer and increase their number in a memory-like pool (van der Windt et al., 2012; van der Windt and Pearce, 2012).

EnPGC-1 is expected to have a negligible effect on tumor cells and to be non-toxic owing to the lower doses (*in vivo* dose 1 mg/kg, equivalent to 3.87 μ M) used in this study (Figure S4E) as shown by similar tumor growth and survival of the control IgG and EnPGC-1-treated group (Figures 4B and 4C). Furthermore, tumor cells are less sensitive to EnPGC-1 for enhancing OCR at physiological ranges (Figure S4F).

The programmable nature of EnPGC-1 allows it to alter its chemical architecture and improve its bioefficacy. Here, we chose CBP30 as the functional ligand of EnPGC-1 owing to its synthetic accessibility of building blocks. While EnPGC-1 demonstrated notable bioactivity, it has limited selectivity over BET bromodomains. Therefore, more specific inhibitors with higher selectivity over BET bromodomains could further enhance bioefficacy. Through the data generated by independent lines of evidence, we suggested the recruitment of p300 acetyltransferase as the mechanism behind EnPGC-1-mediated gene activation. Dancy et al. showed the essential role of the p300/CBP bromodomain for the catalytic activity of their acetyltransferase domain (Zucconi et al., 2016; Dancy et al., 2012). Further studies are warranted to gain deeper insights into whether the modulation of the coactivator binding site interface could indirectly affect EnPGC-1-mediated gene expression. According to our previous report, our epigenetic activator operates through site-specific transcription activation. As shown in Figure 3E, the genome-wide acetylation profile showed a prominent enrichment of H3K27 acetylation in the promoter region of both PGC-1 α and PGC-1 β in CD8⁺ T cells treated with EnPGC-1 and not with DMSO. To clarify, if EnPGC-1 has binding sites in the promoter, we performed sequence alignment of the promoter sequences in human and mouse and observed 65% homology in PGC-1 α , and 63% sequence homology in PGC-1 β . While there are potential binding sites in the notably acetylated region of PGC-1 α and PGC-1 β in EnPGC-1-treated cells (Figure S3F), it is not straightforward to verify the exact homologous sequence targetable by PIP as EnPGC-1 recognizes only six base pairs

and can have cognate binding sites across the entire genome. However, the genome-wide transcriptome analysis showed that the major biological process of EnPGC-1-upregulated genes corresponds to T cell activation (Dpp4 and Tcf7), OXPHOS (Atp10d, Atp1b2), lipid metabolism (Slc12a7 and Cpt1a), and regulation of leukocyte cell to cell adhesion in the EnPGC-1-treated cells. Future studies to advance EnPGC-1 for clinical application need rational design considering the points mentioned and delivering them specifically to T cells by incorporating aptamers and short peptides to reduce their off-target effects (Bai et al., 2020). Because PGC-1 signaling is known to be essential for energy metabolism (Lin et al., 2005; St-Pierre et al., 2003), EnPGC-1 can potentially be developed as a drug not just for enhancing antitumor immunity but also for hyperlipidemia and type 2 diabetes. Although the pharmacokinetics of different versions of PIPs have been studied before (Synold et al., 2012; Fukasawa et al., 2009), the pharmacokinetic properties of EnPGC-1 need to be tested to validate their clinical prospects.

Nevertheless, we have shown that the EnPGC-1-mediated induction of PGC-1 α/β enhances mitochondrial biogenesis and global oxidative metabolism. Our proof-of-concept study substantiates the potential of DNA-based programmable small molecules to control the key regulatory factors associated with T-cell-based immune responses against cancer. PIPs have the potential to be developed to meet the unmet needs in cancer immunotherapy because of their special features, such as their small size, binding to a DNA sequence with an affinity similar to that of a transcription factor, permeability to the cell membrane, cost-effectiveness, solid-phase synthesis, and low or no immunogenicity.

SIGNIFICANCE

Despite the wide success of PD-1 blockade therapy, a significant fraction of cancer patients still do not respond to PD-1-blockade-based monotherapy. Unresponsiveness could be attributed to (1) insufficient number of effector cells due to apoptosis, and (2) reduced PGC-1 expression in effector T cells in the suppressive tumor microenvironment. While epigenetic drugs have shown potential in cancer treatment, lack of programmable nature and sequence selectivity has been major barrier in their clinical use. In this work, we harnessed the selective DNA-binding capability of PIPs and guided an epigenetic reader to enable a targeted epigenetic induction of PGC-1 that regulates mitochondrial biogenesis in CD8⁺ T cells. The epigenetic reader, EnPGC-1, enhances the mitochondrial activation, proliferation, and OXPHOS in CD8⁺ T cells *in vitro*. Furthermore, EnPGC-1 synergizes with PD-1 blockade therapy *in vivo*, enhances the number of tumor-infiltrating CD8⁺ T cells, and skewed their metabolism toward OXPHOS/FAO with memory-like cells having enhanced longevity. Together, this study represents the development of a programmable DNA-based epigenetic drug that could open a new avenue to treat less-responsive cancer patients in combination with PD-1 blockade cancer immunotherapy. Since EnPGC-1 enhances PGC-1 α/β , it may be fine-tuned for treating hyperlipidemia, type 2 diabetes, and OXPHOS-related mitochondrial disorders.

STAR★METHODS

Detailed methods are provided in the online version of this paper and include the following:

- KEY RESOURCES TABLE
- RESOURCE AVAILABILITY
 - Lead contact
 - Materials availability
 - Data and code availability
- EXPERIMENTAL MODEL AND SUBJECT DETAILS
 - Cell lines
 - Animals and study approval
 - *In vivo* PD-1 blockade therapy along with PIP
 - *In vivo* tumor analysis
- METHOD DETAILS
 - PIP synthesis
 - CD8⁺ T cell isolation
 - Flow cytometry analysis
 - Proliferation assay
 - Squelching assay
 - Real-time RT-PCR
 - Mitochondrial DNA copy number assessment
 - siRNA mediated knockdown assay
 - T_m analysis
 - Chromatin immunoprecipitation (ChIP) assay
 - ChIP-sequencing (ChIP-Seq) analysis
 - RNA-seq data generation
 - RNA-seq data analysis
 - Measurement of OCR and ECAR using Seahorse XF analyzer
- QUANTIFICATION AND STATISTICAL ANALYSIS

SUPPLEMENTAL INFORMATION

Supplemental information can be found online at <https://doi.org/10.1016/j.chembiol.2021.08.001>.

ACKNOWLEDGMENTS

We thank Hashiya Kaori, Shuji Ikeda, and Shinsuke Sato for PIP synthesis; Kandarp Joshi for performing the RNA-seq analysis and data visualization; medical support center for providing Seahorse flux analyzer facility; and iCeMS support center, Kyoto University for flow cytometry equipment. This work was supported by AMED (JP20am0101101, Platform Project for Supporting Drug Discovery and Life Science Research [BINDS] to H.S.), 19H03349 (Grants-in-Aid for Scientific Research (B) to G.N.P.), 16H06356 (Grants-in-Aid for Scientific Research (S) to H.S.), 20H05936 (Grant-in-Aid for Transformative Research Areas (A) to H.S.), Takeda Science Foundation (to G.N.P.), Hirose International Foundation (to G.N.P.), and NIH awards (R01CA236350 to H.S.).

AUTHOR CONTRIBUTIONS

Conceptualization, G.N.P. and H.S.; methodology, M.M.; organic synthesis, M.M.; *in vitro* cell assays and *in vivo* experiment, M.M.; analysis and interpretation of data, M.M.; writing – original draft, M.M.; writing – review & editing, G.N.P. and H.S.; supervision, G.N.P. and H.S.

DECLARATION OF INTERESTS

The authors declare no competing interests.

Received: November 6, 2020
Revised: June 4, 2021
Accepted: August 1, 2021
Published: September 13, 2021

REFERENCES

- Azimi, F., Scolyer, R.A., Rumcheva, P., Moncrieff, M., Murali, R., McCarthy, S.W., Saw, R.P., and Thompson, J.F. (2012). Tumor-infiltrating lymphocyte grade is an independent predictor of sentinel lymph node status and survival in patients with cutaneous melanoma. *J. Clin. Oncol.* **30**, 2678–2683.
- Bai, C., Gao, S., Hu, S., Liu, X., Li, H., Dong, J., Huang, A., Zhu, L., Zhou, P., Li, S., and Shao, N. (2020). Self-assembled multivalent aptamer nanoparticles with potential CAR-like characteristics could activate T cells and inhibit melanoma growth. *Mol. Ther. Oncolytics* **17**, 9–20.
- Buck, M.D., O'sullivan, D., Klein Geltink, R.I., Curtis, J.D., Chang, C.H., Sanin, D.E., Qiu, J., Kretz, O., Braas, D., Van Der Windt, G.J., et al. (2016). Mitochondrial dynamics controls T cell fate through metabolic programming. *Cell* **166**, 63–76.
- Buck, M.D., Sowell, R.T., Kaech, S.M., and Pearce, E.L. (2017). Metabolic instruction of immunity. *Cell* **169**, 570–586.
- Chamoto, K., Chowdhury, P.S., Kumar, A., Sonomura, K., Matsuda, F., Fagarasan, S., and Honjo, T. (2017). Mitochondrial activation chemicals synergize with surface receptor PD-1 blockade for T cell-dependent antitumor activity. *Proc. Natl. Acad. Sci. U S A* **114**, E761–E770.
- Chamoto, K., Hatae, R., and Honjo, T. (2020). Current issues and perspectives in PD-1 blockade cancer immunotherapy. *Int. J. Clin. Oncol.* **25**, 790–800.
- Choi, J.M., and Bothwell, A.L. (2012). The nuclear receptor PPARs as important regulators of T-cell functions and autoimmune diseases. *Mol. Cells* **33**, 217–222.
- Chowdhury, P.S., Chamoto, K., Kumar, A., and Honjo, T. (2018). PPAR-induced fatty acid oxidation in T cells increases the number of tumor-reactive CD8(+) T cells and facilitates anti-PD-1 therapy. *Cancer Immunol. Res.* **6**, 1375–1387.
- Couzin-Frankel, J. (2013). Breakthrough of the year 2013. Cancer immunotherapy. *Science* **342**, 1432–1433.
- Dancy, B.M., Crump, N.T., Peterson, D.J., Mukherjee, C., Bowers, E.M., Ahn, Y.-H., Yoshida, M., Zhang, J., Mahadevan, L.C., Meyers, D.J., et al. (2012). Live-cell studies of p300/CBP histone acetyltransferase activity and inhibition. *ChemBioChem* **13**, 2113–2121.
- Dervan, P.B., and Edelson, B.S. (2003). Recognition of the DNA minor groove by pyrrole-imidazole polyamides. *Curr. Opin. Struct. Biol.* **13**, 284–299.
- Dunn, G.P., Old, L.J., and Schreiber, R.D. (2004). The immunobiology of cancer immunosurveillance and immunoediting. *Immunity* **21**, 137–148.
- Fife, B.T., and Bluestone, J.A. (2008). Control of peripheral T-cell tolerance and autoimmunity via the CTLA-4 and PD-1 pathways. *Immunol. Rev.* **224**, 166–182.
- Fukasawa, A., Aoyama, T., Nagashima, T., Fukuda, N., Ueno, T., Sugiyama, H., Nagase, H., and Matsumoto, Y. (2009). Pharmacokinetics of pyrrole-imidazole polyamides after intravenous administration in rat. *Biopharm. Drug Dispos.* **30**, 81–89.
- Gallagher, S.J., Shklovskaya, E., and Hersey, P. (2017). Epigenetic modulation in cancer immunotherapy. *Curr. Opin. Pharmacol.* **35**, 48–56.
- Han, L., Pandian, G.N., Chandran, A., Sato, S., Taniguchi, J., Kashiwazaki, G., Sawatani, Y., Hashiya, K., Bando, T., Xu, Y., et al. (2015). A synthetic DNA-binding domain guides distinct chromatin-modifying small molecules to activate an identical gene network. *Angew. Chem. Int. Ed.* **54**, 8700–8703.
- Hatae, R., Chamoto, K., Kim, Y.H., Sonomura, K., Taneishi, K., Kawaguchi, S., Yoshida, H., Ozasa, H., Sakamori, Y., Akrami, M., et al. (2020). Combination of host immune metabolic biomarkers for the PD-1 blockade cancer immunotherapy. *JCI Insight* **5**, e133501.
- Hidaka, T., Tsubono, Y., Hashiya, K., Bando, T., Pandian, G.N., and Sugiyama, H. (2020). Enhanced nuclear accumulation of pyrrole-imidazole polyamides by incorporation of the tri-arginine vector. *Chem. Commun.* **56**, 12371–12374.
- Hiraoka, K., Inoue, T., Taylor, R.D., Watanabe, T., Koshikawa, N., Yoda, H., Shinohara, K.-I., Takatori, A., Sugimoto, H., Maru, Y., et al. (2015). Inhibition of KRAS codon 12 mutants using a novel DNA-alkylating pyrrole-imidazole polyamide conjugate. *Nat. Commun.* **6**, 6706.
- Idos, G.E., Kwok, J., Bonthala, N., Kysh, L., Gruber, S.B., and Qu, C. (2020). The prognostic implications of tumor infiltrating lymphocytes in colorectal cancer: a systematic review and meta-analysis. *Sci. Rep.* **10**, 3360.
- Iwai, Y., Ishida, M., Tanaka, Y., Okazaki, T., Honjo, T., and Minato, N. (2002). Involvement of PD-L1 on tumor cells in the escape from host immune system and tumor immunotherapy by PD-L1 blockade. *Proc. Natl. Acad. Sci. U S A* **99**, 12293–12297.
- Juneja, V.R., Mcguire, K.A., Manguso, R.T., Lafleur, M.W., Collins, N., Haining, W.N., Freeman, G.J., and Sharpe, A.H. (2017). PD-L1 on tumor cells is sufficient for immune evasion in immunogenic tumors and inhibits CD8 T cell cytotoxicity. *J. Exp. Med.* **214**, 895–904.
- Kobayashi, H., Hatakeyama, H., Nishimura, H., Yokota, M., Suzuki, S., Tomabechi, Y., Shirouzu, M., Osada, H., Mimaki, M., Goto, Y.-I., and Yoshida, M. (2021). Chemical reversal of abnormalities in cells carrying mitochondrial DNA mutations. *Nat. Chem. Biol.* **17**, 335–343.
- Kressler, D., Schreiber, S.N., Knutti, D., and Kralli, A. (2002). The PGC-1-related protein PERC is a selective coactivator of estrogen receptor alpha. *J. Biol. Chem.* **277**, 13918–13925.
- Kumar, A., and Chamoto, K. (2021). Immune metabolism in PD-1 blockade-based cancer immunotherapy. *Int. Immunol.* **33**, 17–26.
- Kumar, A., Chamoto, K., Chowdhury, P.S., and Honjo, T. (2020). Tumors attenuating the mitochondrial activity in T cells escape from PD-1 blockade therapy. *eLife* **9**, e52330. <https://doi.org/10.7554/eLife.52330>.
- Leach, D.R., Krummel, M.F., and Allison, J.P. (1996). Enhancement of anti-tumor immunity by CTLA-4 blockade. *Science* **271**, 1734–1736.
- Lin, J., Handschin, C., and Spiegelman, B.M. (2005). Metabolic control through the PGC-1 family of transcription coactivators. *Cell Metab.* **1**, 361–370.
- Lin, J., Puigserver, P., Donovan, J., Tarr, P., and Spiegelman, B.M. (2002). Peroxisome proliferator-activated receptor gamma coactivator 1beta (PGC-1beta), a novel PGC-1-related transcription coactivator associated with host cell factor. *J. Biol. Chem.* **277**, 1645–1648.
- Mahmoud, S.M., Paish, E.C., Powe, D.G., Macmillan, R.D., Grainge, M.J., Lee, A.H., Ellis, I.O., and Green, A.R. (2011). Tumor-infiltrating CD8+ lymphocytes predict clinical outcome in breast cancer. *J. Clin. Oncol.* **29**, 1949–1955.
- Malinee, M., Kumar, A., Hidaka, T., Horie, M., Hasegawa, K., Pandian, G.N., and Sugiyama, H. (2020). Targeted suppression of metastasis regulatory transcription factor SOX2 in various cancer cell lines using a sequence-specific designer pyrrole-imidazole polyamide. *Bioorg. Med. Chem.* **28**, 115248.
- Pandian, G.N., Sato, S., Anandhakumar, C., Taniguchi, J., Takashima, K., Syed, J., Han, L., Saha, A., Bando, T., Nagase, H., and Sugiyama, H. (2014a). Identification of a small molecule that turns ON the pluripotency gene circuitry in human fibroblasts. *ACS Chem. Biol.* **9**, 2729–2736.
- Pandian, G.N., Taniguchi, J., Junetha, S., Sato, S., Han, L., Saha, A., Anandhakumar, C., Bando, T., Nagase, H., Vijayanthi, T., et al. (2014b). Distinct DNA-based epigenetic switches trigger transcriptional activation of silent genes in human dermal fibroblasts. *Sci. Rep.* **4**, 3843.
- Patsoukis, N., Bardhan, K., Chatterjee, P., Sari, D., Liu, B., Bell, L.N., Karoly, E.D., Freeman, G.J., Petkova, V., Seth, P., et al. (2015). PD-1 alters T-cell metabolic reprogramming by inhibiting glycolysis and promoting lipolysis and fatty acid oxidation. *Nat. Commun.* **6**, 6692.
- Paumen, M.B., Ishida, Y., Han, H., Muramatsu, M., Eguchi, Y., Tsujimoto, Y., and Honjo, T. (1997). Direct interaction of the mitochondrial membrane protein carnitine palmitoyltransferase I with Bcl-2. *Biochem. Biophys. Res. Commun.* **231**, 523–525.
- Pearce, E.L. (2010). Metabolism in T cell activation and differentiation. *Curr. Opin. Immunol.* **22**, 314–320.
- Pearce, E.L., Walsh, M.C., Cejas, P.J., Harms, G.M., Shen, H., Wang, L.-S., Jones, R.G., and Choi, Y. (2009). Enhancing CD8 T-cell memory by modulating fatty acid metabolism. *Nature* **460**, 103–107.

- Perianayagam, M.C., Madias, N.E., Pereira, B.J., and Jaber, B.L. (2006). CREB transcription factor modulates Bcl2 transcription in response to C5a in HL-60-derived neutrophils. *Eur. J. Clin. Invest.* **36**, 353–361.
- Picca, A., and Lezza, A.M. (2015). Regulation of mitochondrial biogenesis through TFAM-mitochondrial DNA interactions: useful insights from aging and calorie restriction studies. *Mitochondrion* **25**, 67–75.
- Puigserver, P., Wu, Z., Park, C.W., Graves, R., Wright, M., and Spiegelman, B.M. (1998). A cold-inducible coactivator of nuclear receptors linked to adaptive thermogenesis. *Cell* **92**, 829–839.
- Refinetti, P., Warren, D., Morgenthaler, S., and Ekström, P.O. (2017). Quantifying mitochondrial DNA copy number using robust regression to interpret real time PCR results. *BMC Res. Notes* **10**, 593.
- Scharping, N.E., Menk, A.V., Moreci, R.S., Whetstone, R.D., Dadey, R.E., Watkins, S.C., Ferris, R.L., and Delgoffe, G.M. (2016). The tumor microenvironment represses T cell mitochondrial biogenesis to drive intratumoral T cell metabolic insufficiency and dysfunction. *Immunity* **45**, 701–703.
- Schroder, K., Hertzog, P.J., Ravasi, T., and Hume, D.A. (2004). Interferon-gamma: an overview of signals, mechanisms and functions. *J. Leukoc. Biol.* **75**, 163–189.
- Sena, L.A., Li, S., Jairaman, A., Prakriya, M., Ezponda, T., Hildeman, D.A., Wang, C.R., Schumacker, P.T., Licht, J.D., Perlman, H., et al. (2013). Mitochondria are required for antigen-specific T cell activation through reactive oxygen species signaling. *Immunity* **38**, 225–236.
- Shao, S., Xu, Q., Yu, X., Pan, R., and Chen, Y. (2020). Dipeptidyl peptidase 4 inhibitors and their potential immune modulatory functions. *Pharmacol. Ther.* **209**, 107503.
- St-Pierre, J., Lin, J., Krauss, S., Tarr, P.T., Yang, R., Newgard, C.B., and Spiegelman, B.M. (2003). Bioenergetic analysis of peroxisome proliferator-activated receptor gamma coactivators 1alpha and 1beta (PGC-1alpha and PGC-1beta) in muscle cells. *J. Biol. Chem.* **278**, 26597–26603.
- Synold, T.W., Xi, B., Wu, J., Yen, Y., Li, B.C., Yang, F., Phillips, J.W., Nickols, N.G., and Dervan, P.B. (2012). Single-dose pharmacokinetic and toxicity analysis of pyrrole-imidazole polyamides in mice. *Cancer Chemother. Pharmacol.* **70**, 617–625.
- Takahashi, T., Asami, Y., Kitamura, E., Suzuki, T., Wang, X., Igarashi, J., Morohashi, A., Shinjima, Y., Kanou, H., Saito, K., et al. (2008). Development of pyrrole-imidazole polyamide for specific regulation of human aurora kinase-A and -B gene expression. *Chem. Biol.* **15**, 829–841.
- Taniguchi, J., Feng, Y., Pandian, G.N., Hashiya, F., Hidaka, T., Hashiya, K., Park, S., Bando, T., Ito, S., and Sugiyama, H. (2018). Biomimetic artificial epigenetic code for targeted acetylation of histones. *J. Am. Chem. Soc.* **140**, 7108–7115.
- Topalian, S.L., Drake, C.G., and Pardoll, D.M. (2015). Immune checkpoint blockade: a common denominator approach to cancer therapy. *Cancer Cell* **27**, 450–461.
- Turner, B.M. (1991). Histone acetylation and control of gene expression. *J. Cell Sci.* **99**, 13–20.
- Vaijyanthi, T., Bando, T., Pandian, G.N., and Sugiyama, H. (2012). Progress and prospects of pyrrole-imidazole polyamide-fluorophore conjugates as sequence-selective DNA probes. *ChemBioChem* **13**, 2170–2185.
- van der Windt, G.J., Everts, B., Chang, C.H., Curtis, J.D., Freitas, T.C., Amiel, E., Pearce, E.J., and Pearce, E.L. (2012). Mitochondrial respiratory capacity is a critical regulator of CD8+ T cell memory development. *Immunity* **36**, 68–78.
- van der Windt, G.J., O'sullivan, D., Everts, B., Huang, S.C., Buck, M.D., Curtis, J.D., Chang, C.H., Smith, A.M., Ai, T., Faubert, B., et al. (2013). CD8 memory T cells have a bioenergetic advantage that underlies their rapid recall ability. *Proc. Natl. Acad. Sci. U S A* **110**, 14336–14341.
- van der Windt, G.J., and Pearce, E.L. (2012). Metabolic switching and fuel choice during T-cell differentiation and memory development. *Immunol. Rev.* **249**, 27–42.
- Verdone, L., Agricola, E., Caserta, M., and Di Mauro, E. (2006). Histone acetylation in gene regulation. *Brief. Funct. Genomics* **5**, 209–221.
- Villena, J.A., and Kralli, A. (2008). ERRalpha: a metabolic function for the oldest orphan. *Trends Endocrinol. Metab.* **19**, 269–276.
- Wan, H., Xu, B., Zhu, N., and Ren, B. (2020). PGC-1 α activator-induced fatty acid oxidation in tumor-infiltrating CTLs enhances effects of PD-1 blockade therapy in lung cancer. *Tumori* **106**, 55–63.
- Wang, Y., An, H., Liu, T., Qin, C., Sesaki, H., Guo, S., Radovick, S., Hussain, M., Maheshwari, A., Wondisford, F.E., et al. (2019). Metformin improves mitochondrial respiratory activity through activation of AMPK. *Cell Rep.* **29**, 1511–1523.e5.
- Weinberg, S.E., Sena, L.A., and Chandel, N.S. (2015). Mitochondria in the regulation of innate and adaptive immunity. *Immunity* **42**, 406–417.
- Zhu, H., Bengsch, F., Svoronos, N., Rutkowski, M.R., Bitler, B.G., Allegranza, M.J., Yokoyama, Y., Kossenkov, A.V., Bradner, J.E., Conejo-Garcia, J.R., and Zhang, R. (2016). BET bromodomain inhibition promotes anti-tumor immunity by suppressing PD-L1 expression. *Cell Rep.* **16**, 2829–2837.
- Zou, W., Wolchok, J.D., and Chen, L. (2016). PD-L1 (B7-H1) and PD-1 pathway blockade for cancer therapy: mechanisms, response biomarkers, and combinations. *Sci. Transl. Med.* **8**, 328rv4.
- Zucconi, B.E., Luef, B., Xu, W., Henry, R.A., Nodelman, I.M., Bowman, G.D., Andrews, A.J., and Cole, P.A. (2016). Modulation of p300/CBP acetylation of nucleosomes by bromodomain ligand I-CBP112. *Biochemistry* **55**, 3727–3734.

STAR★METHODS

KEY RESOURCES TABLE

REAGENT or RESOURCE	SOURCE	IDENTIFIER
Antibodies		
anti-PD-L1 mAb (clone 10F.9G2)	BioXcell	Cat# BE0101
Rat IgG2b, k (clone RTK4530)	Biologend	Cat# 400607
anti-CD3 mAb (clone 145.2C11)	Biologend	Cat#100339
CD28 mAb (clone 37.51)	eBioscience	Cat#16-0281-85
CD8 (clone 53-6.7)	Biologend	N/A
CD62L (clone MEL-14)	Biologend	N/A
CD44 (clone IM7)	Biologend	N/A
CD45.2 (clone 104)	Biologend	N/A
Ki67 mAb (clone solA15)	eBioscience	N/A
IFN gamma mAb (clone XMG-1.2)	Biologend	N/A
PGC-1 α/β	Abcam	Cat# Ab72230
Rabbit pAb isotype control	Abcam,	Cat# ab37415
anti-mouse KAT3B/p300 mAb	Abcam	Cat# ab54984
anti-mouse H3K27Ac	Abcam	Cat# ab4729
anti-mouse histone H4 acetylated (pan-acetyl)	Active motif	Cat# 39925
Dynabeads protein G	Thermo Fisher Scientific	Cat#10004D
Chemicals, peptides, and recombinant proteins		
Naïve CD8 T cell isolation kit	Biologend,	Cat# 480043
FOXP3 staining kit	Invitrogen	Cat#00-5523-00
Cell trace violet cell proliferation kit	Life technologies	Cat#C34557
ChIP-IT PBMC kit	Active Motif,	Cat# 53042
QIAamp DNA mini kit	Qiagen	Cat# 51304
RNA isolation kit (Fast Gene)	Nippon genetics	Cat# FG -80250
RNeasy mini kit	QIAGEN	Cat# 74106
ReverTrace qPCR RT kit	Toyobo	Cat#FSQ-101
THUNDERBIRD SYBR qPCR Mix	Toyobo	Cat#QPS-201
gDNA remover	Toyobo	Cat#FSQ-301
nucleofector medium	Amaxa,	Cat# VZB-1001
SGC-CBP30	MedChemExpress	Cat#HY-15826
A-485	MedChemExpress	Cat#HY-107455
Dulbecco's Modified Eagle Medium	Thermo Fisher Scientific	Cat# 10569010
RPMI 1640	Gibco	Cat# 11875-093
Fetal bovine serum (FBS)	Sigma	Cat# 173012
Pen/Strep	Nacalai tesck	Cat# 26253-84
Critical commercial assays		
MitoTracker Green	Life Technologies, CA	N/A
MitoTracker Deep Red	Life Technologies, CA	N/A
MitoSOX Red (Mitochondrial superoxide indicator)	Life Technologies, CA	Cat#M36008
CellROX Green reagents	Life Technologies, CA	N/A
Fatty Acid Oxidation Detection Reagent	Funakoshi,	Cat# FDV-0033
XFe96 Extracellular Flux analyzer	Seahorse Biosciences, USA	N/A
XF cell Mito Stress Test Kit	Seahorse Biosciences, USA	Cat# 103015-100
Deposited data		
RNA-sequencing data (Macrogen Japan)	This paper	GSE174750, https://www.ncbi.nlm.nih.gov/geo/
ChIP-sequencing data (Macrogen Japan)	This paper	GSE175849, https://www.ncbi.nlm.nih.gov/geo/

(Continued on next page)

Continued

REAGENT or RESOURCE	SOURCE	IDENTIFIER
Experimental models: cell lines		
Murine: MC38 (murine colorectal carcinoma)	Kerafast Inc, U.S.	Cat# ENH204-FP
Murine: B16 melanoma	ATCC	N/A
Human: HDF (human dermal fibroblast)	Cell Application, INC	N/A
iPS-induced cardiomyocytes	This paper	N/A
Experimental models: organisms/strains		
C57BL/6N	CLEA Japan (Tokyo, Japan)	N/A
Oligonucleotides		
siPGC-1 α , CACAACUCCUCCUCAUAAAAdTdT	Sigma Aldrich	N/A
siPGC-1 β , CUCAUUCGCUACAUGCAUAdTdT	Sigma Aldrich	N/A
siCtrl, GAAUACUCUACAAACCCUCdTdT	Sigma Aldrich	N/A
EnPGC1-DNA, 5'-GGCAGCCTCGG-3'	This paper	N/A
Mismatch-DNA, 5'-GGCAGACGTCGG-3'	This paper	N/A
Software and algorithms		
Neon™ Transfection System (Serial No:922963)	Life Science Technologies	https://www.thermofisher.com/us/en/home.html
Seahorse XFe96 Analyzer	Agilent Technologies	https://www.agilent.com/
LightCycler® 480 Software, Version 1.5	Roche Life Science	https://lifescience.roche.com/en_us.html
BD LSRFortessa Cel Analyzer	BD Bioscience	https://www.bdbiosciences.com/en-in
FlowJo	LLC, Becton Dickinson	https://www.flowjo.com/solutions/flowjo
Ultrasonicator S220	Covaris	https://www.covaris.com/
Prism	GraphPad	https://www.graphpad.com/scientific-software/prism/

RESOURCE AVAILABILITY

Lead contact

Further information and requests for resources and reagents should be directed to and will be fulfilled by the lead contact, Hiroshi Sugiyama (hs@kuchem.kyoto-u.ac.jp).

Materials availability

Compounds generated in this study will be made available upon reasonable request.

Data and code availability

- RNA-sequencing and ChIP-sequencing data has been deposited at Gene Expression Omnibus (GEO) repository (<http://www.ncbi.nlm.nih.gov/geo>).
- All original code has been deposited at GEO repository and is publicly available as of the date of publication. DOIs are listed in the key resources table.
- Any additional information required to reanalyze the data reported in this paper is available from the lead contact upon request.

EXPERIMENTAL MODEL AND SUBJECT DETAILS

Cell lines

Cell lines were cultured in DMEM (Gibco, Catalog # 10569-010), RPMI 1640 (Gibco, Catalog # 11875-093) media supplemented with 1% Pen/Strep (nacalai tesck, Catalog # 26253-84) and 10% heat-inactivated fetal bovine serum (FBS) according to the ATCC recommendations. Cell lines were free from mycoplasma contamination and were monitored regularly for contamination. Cell cultures were maintained at 37°C with 5% CO₂ in a humidified incubator. Cell cultures were used within four passages for all the experiments in this work. MC38 (murine colorectal carcinoma cell line from C57BL/6N background) cell line was bought from Kerafast Inc, U.S. B16 (murine melanoma cell line from C57BL/6N background) and HDF (human dermal fibroblast) were purchased from ATCC. PIPs were added at the conc. of 5 μ M for *in vitro* assays throughout this work wherever it is used unless specified.

Animals and study approval

6-8 weeks old female C57BL/6N mice were purchased from 'CLEA Japan (Tokyo, Japan)' and maintained under specific pathogen-free conditions at the 'Laboratory Animal Research Center, iCeMS, Kyoto University' under the direction of the Institutional Review Board, Kyoto University.

In vivo PD-1 blockade therapy along with PIP

MC38 (0.5 million cells) tumor cells were intradermally (i.d.) injected into the right flank of C57BL/6N mice (day 0). On day 6, combination therapy was started. Anti-PD-L1 mAb (40 μ g per mouse, clone 10F.9G2, BioXcell, Catalog# BE0101) and the PIPs EnPGC-1 and other controls (1mg/kg) were injected intraperitoneally (i.p.). PIPs were injected every third day and anti-PD-L1 mAb every sixth days. Therapy was performed up to one month and survival was recorded. Tumor size was measured alternate days using a caliper and tumor volume was calculated using the formula for a typical ellipsoid. For control group, an isotype control for the anti-PD-L1 mAb (Rat IgG2b, k) was injected. Related to [Figure 4](#).

In vivo tumor analysis

Three tumor DLN (tDLN) were harvested and homogenized to make single cell suspension. Absolute number of lymphocytes (number of lymphocytes per DLN) were calculated. DLN cells were stained with anti-CD8, anti-CD62L and anti-CD44 mAbs. CD8⁺ DLN cells were further extrapolated based on the intensity of CD62L and CD44 and were classified in different CD8⁺ T cell subsets (naïve, CD62L^{high} CD44^{low}; central memory, CD62L^{high} CD44^{high}; and effector memory, CD62L^{low} CD44^{high}). Related to [Figure 4](#).

METHOD DETAILS

PIP synthesis

EnPGC-1 was synthesized according to the procedures described previously ([Hidaka et al., 2020](#); [Taniguchi et al., 2018](#)). In brief, Fmoc solid-phase synthesis of designed PIP structures was performed on a PSSM-8 (Shimadzu), then cleavage was carried out with 1 ml of 3,3-diamino-N-methylpropylamine (Dp) for 3 h at 45 °C. The resulting crude PIPs were purified by flash column chromatography. The purified PIPs were then characterized by HPLC and MALDI-TOF/MS. Chemical structure of each PIPs used in this work have been shown with respective HPLC chart and mass spectra in [Figures S1G–S1J](#).

CD8⁺ T cell isolation

Naïve CD8⁺ T (CD62L^{high} CD44^{low}) cells were purified from pooled lymphocytes of lymph nodes (axillary, brachial, and inguinal LNs) and spleen from 6-8 weeks old C57BL/6N inbred wild-type female mice. Spleen cells were treated with ACK lysis buffer (0.15 M NH₄Cl + 1.0 mM KHCO₃ + 0.1 mM Na₂-EDTA) for 2 min to lyse the erythrocytes before pooling into lymph node cells. Naïve CD8⁺ T cells were purified following manufacturer's instructions (Biolegend, Catalog# 480043). For *in vitro* analysis, naïve CD8⁺ T cells were stimulated with 1 μ g/ml conc. of each anti-CD3 mAb (clone 145.2C11, Biolegend, Catalog#100339) and anti-CD28 mAb (clone 37.51, eBioscience, Catalog#16-0281-85). CD8⁺ T cells were cultured in 'Spleen RPMI media' (RPMI with 10% FCS, 1% Pen/Strep mix, 1% nonessential amino acids, 50 μ M β -mercaptoethanol, 2 mM L-Glutamine, and 1% sodium pyruvate) in all the *in vitro* experiments throughout this project. Naïve CD8⁺ T (CD62L^{high} CD44^{low}) cells (100 thousand cell/ well) were seeded in 96-well round bottom plate and stimulated with anti-CD3 and anti-CD28 mAbs (each 1 μ g/mL conc.). PIPs were added 5 μ M or indicated conc. and incubated for 48 h are used for all the downstream analysis.

Flow cytometry analysis

PGC-1 α/β protein level quantification

Murine primary CD8⁺ T cells were given TCR stimulation (with anti-CD3/CD28 mAb) and treated with EnPGC-1 or other control PIPs as per the schedule mentioned in [Figure 1B](#) and protein level of PGC-1 α/β was quantified intranuclearly (Foxp3 staining kit). For staining PGC-1, the previously reported anti-PGC-1 α/β antibody (Abcam, ab72230) was used that detects both PGC-1 α and PGC-1 β human/mice ([Hatae et al., 2020](#); [Wang et al., 2019](#)). Isotype control antibodies were used as staining control. Related to [Figure 1E](#).

Mitochondrial activation assessment

Mitochondrial activation parameters e.g., potential, mass, and ROS generation were assessed using vital dyes MitoTracker Deep Red, MitoTracker Green, MitoSOX Red/CellROX (Life Technologies). The conc. of dyes was used as per recommendation. Cells were incubated with dyes for 30 minutes followed by wash with PBS and surface staining, if any, e.g., CD45.2 (104, Biolegend), CD44 (IM7, Biolegend), CD8 (53-6.7, Biolegend), CD62L (MEL-14, Biolegend). Related to [Figure 2A](#) and [4G](#).

Fatty acid oxidation measurement

FAO was assessed using 'Fatty Acid Oxidation Detection Reagent' (FAOBlue) (Funakoshi, Catalog#FDV-0033). Cells were first washed twice with D-PBS followed by addition of FAOBlue (15 μ M in serum-free RPMI media) and incubated for 2 h at 37 °C in a 5% CO₂ humidified incubator. After incubation, cells were centrifuged, washed twice with D-PBS and further stained for surface proteins (if any) and analyzed by flow cytometry under brilliant violet laser. Related to [Figure 4K](#).

Cytokine intracellular staining

For intracellular staining, cells were first surface stained (if any) before moving to the fixation and permeabilization step. After surface staining and washing with FACS buffer (PBS, 0.5-1% BSA or 5-10% FBS, 0.1% NaN₃ sodium azide), cells were fixed using

polyparaformaldehyde solution (1.5% in D-PBS; 30 minutes incubation at 4 °C). Cells were washed using FACS buffer followed by permeabilization using Triton-X solution (0.5% Triton-X-100 in PBS; 30 minutes incubation at 4 °C). Following the incubation, cells were washed with FACS buffer and stained with antibodies against the target protein of interest e.g., Ki67 (clone SolA15, eBioscience), IFN- γ clone XMG-1.2, Biolegend). Related to [Figure 4J](#).

Proliferation assay

Naïve CD8⁺ T cells were isolated and labelled with CellTrace Violet (CTV) (1 μ M in PBS suspension, 15 minutes, 37 °C.). Staining was quenched with FBS containing media and washed 2 times with FBS containing media. Further, 100 thousand cells were seeded in 96-well round bottom plate and stimulated with anti-CD3/CD28 mAbs (each 1 μ g/ml). PIPs were added and incubated for 72 h. 72 h post stimulation was considered as good time point to assess proliferation by dye dilution method or by Ki67 (a proliferation marker) staining method. Related to [Figures 2D](#) and [2E](#).

Squelching assay

Naïve CD8⁺ T cells were harvested from C57BL/6N mice and TCR stimulated with anti-CD3/anti-CD28 mAbs. In addition, PIP (5 μ M) and different doses of SGC-CBP30 (CBP/p300 inhibitor) and A-485 (p300 acetyltransferase inhibitor) were added and stimulated for 48 h. Based on our initial optimization experiments with a range (100 nM-1000 nM) of conc., we chose the working conc. of SGC-CBP30 as 200 nM as a notable cytotoxicity was observed from 500 nM. Likewise, a range of conc. (1-50 nM) were tested for A-485 and we chose to work with 5 nM to clarify the mechanism of inhibition as no notable fold change observed beyond 10 nM. Related to [Figures 1F–1G](#), [S1E](#), and [S1F](#).

Real-time RT-PCR

Total RNA was isolated by using RNeasy mini kit (QIAGEN) and generated cDNA by reverse transcription (Invitrogen). 1 μ g of total RNA was reverse transcribed into cDNA by ReverTraAce qPCR RTMasterMix with gDNA Remover (Toyobo) and qPCR was performed using THUNDERBIRD SYBR qPCR Mix (Toyobo) in LightCycler 480 (Roche Diagnostics GmbH). 20ng cDNA were run for qPCR analysis. Cp value was determined by the second derivative maximum method and relative RNA amount was calculated. As an internal control, Gapdh was used. The list of the primers used in this work is listed in [Table S1](#).

Mitochondrial DNA copy number assessment

Mitochondrial DNA (mtDNA) copy number was assessed in CD8⁺ T cells treated with EnPGC-1 (5 μ M) or DMSO vehicle. DNA extractions were performed using a QIAamp DNA mini kit (Qiagen). qPCR was performed to measure the mtDNA copy numbers, using mtDNA-encoded NADH dehydrogenase 1 (ND1) ([Refinetti et al., 2017](#)). The abundance of target gene was normalized to the signal for nuclear hexokinase 2 (HK2) gene. Related to [Figure 2F](#).

siRNA mediated knockdown assay

Purified CD8⁺ T cells were electroporated with siRNAs against PGC-1 α and PGC-1 β using neon electroporation system. The protocol was followed according to manufacturer's instructions for primary T cells. 10 pico mole of siRNA were used per 1 million cells. Electroporated cells were incubated for 6 h in complete nucleofector medium (Amaxa, Catalog# VZB-1001) followed by TCR stimulation (anti-CD3/CD28 mAbs) and PIP (5 μ M) treatment. The cells were incubated for 48 h. Following the incubation, cells were harvested, RNA purified, and qPCR was performed (GAPDH was used as loading control). The sequence of siRNA used were as follows: siPGC-1 α , CACAACUCCUCCUCAUAAAdTdT; siPGC-1 β , CUCAUUCGCUACAUGCAUAdTdT; siCtrl, CAAUACUCUACAAACCCUCdTdT. The siRNA sequences have been listed in [Table S1](#). Related to [Figures 3A–3C](#) and [S3A](#).

T_m analysis

Two DNA oligomers (5'-GGCAGCCTCGG-3' (EnPGC1-DNA), and 5'-GGCAGACGTCGG-3' (Mismatch-DNA)) used in this analysis were purchased from Sigma. The analytical buffer for T_m analysis was aqueous solution of 10 mM sodium chloride and 10 mM Tris-HCl at pH 7.5 containing 0.5% v/v DMSO. The conc. of dsDNA was 2.5 μ M. The conc. of polyamides was 5 μ M (2 equiv.). Further, samples were annealed from 95°C to 20°C (dsDNA with PIP) or 95°C–5°C (DNA only) at 1.0°C/min. Absorbance at 260 nm was recorded from 20°C to 95°C (dsDNA with PIP) or 5°C–95°C (DNA only) at a rate of 1.0°C/min using a spectrophotometer V-650 or V-750 (JASCO) with a thermo-controlled PAC-743R cell changer (JASCO) and a thermal-circulator F25-ED or CTU-100 (JASCO). The T_m values are shown in [Figure S3B](#). The T_m values are the average of technical triplicates and SD were calculated. The template DNA sequences have been listed in [Table S1](#) and the assay is related to [Figure S3B](#).

Chromatin immunoprecipitation (ChIP) assay

Murine primary CD8⁺ T cells were TCR stimulated (anti-CD3/anti-CD28 mAb) and treated with PIP (5 μ M) for 48 h. ChIP assay for CD8⁺ T cells was performed using ChIP-IT PBMC kit following manufacturer's protocol (Active Motif, Catalog#53042). For ChIP using B16 cells, 0.5 million cells per 90 mm dish were seeded and next day treated with PIPs for 48 h. Following the treatment, cells were collected, and cross-linking was performed (with 1% formaldehyde, 10 min incubation at RT). 125 mM glycine was then added to stop the reaction. Cells were washed once with PBS and then lysed in Lysis buffer (10 mM Tris-HCl (pH 7.5), 200 mM NaCl, 10 mM EDTA, 1% (v/v) SDS, supplemented with complete protease inhibitor cocktail (Roche)). The chromatin was then sheared

with an ultrasonicator (Covaris, S2). The sheared chromatin was electrophoresed on agarose gel to check the fragment size (Figure S3C). Insoluble precipitates were removed by centrifugation (16,000 g, 10 min, 4°C). The sheared chromatin was diluted three times in IP buffer (16.7 mM Tris-HCl, 1.2 mM EDTA, 1.1% (v/v) Triton X-100, 167 mM NaCl, 0.01% (v/v) SDS, pH 8.0, supplemented with cOmplete) and precleared with dynabeads protein G (Thermo S20 Fisher Scientific) at 4°C. To 500 μ L of precleared chromatin, 50 μ L of protein G dynabeads and 10 μ L of the Rabbit pAb isotype control (Abcam, Catalog#ab37415), anti-mouse KAT3B/p300 mAb (Abcam, Catalog# ab54984), anti-mouse H3K27Ac (Abcam, Catalog# ab4729), and anti-mouse histone H4 acetylated (pan-acetyl) (Active motif, Catalog# 39,925) were added. Immunoprecipitation was then performed by incubating the mixture for overnight at 4°C. The beads were then washed once with IP buffer, twice with Wash 1 buffer (20 mM Tris-HCl, 2 mM EDTA, 1.1% (v/v) Triton X-100, 0.1% (v/v) SDS, 150 mM NaCl, pH 8.0), twice with Wash 2 buffer (20 mM Tris-HCl, 2 mM EDTA, 1.1% (v/v) Triton X-100, 0.1% (v/v) SDS, 500 mM NaCl, pH 8.0), twice with Wash 3 buffer (10 mM Tris-HCl, 1 mM EDTA, 250 mM LiCl, 1% (v/v) NP-40, 1% (w/v) sodium deoxycholate, pH 8.0), and twice with TE buffer (10 mM Tris-HCl, 1 mM EDTA, pH 8.0), and then were suspended in 200 μ L of Reverse cross-linking buffer (100 mM NaHCO₃, 1% (v/v) SDS). The suspension was supplemented with 1.5 mg/mL of pronase (Sigma Aldrich) and shaken at 42°C for 2 h, then at 65°C overnight. For input samples, the precleared chromatin was directly reverse cross-linked without immunoprecipitation. DNA was purified using QIAquick PCR Purification Kit (Qiagen) and quantified by Bioanalyzer (Agilent Technologies) using Agilent High Sensitivity DNA Kit (Agilent Technologies). ChIP products were subjected to PCR-based amplification with the indicated primer sets (see Table S1). ChIP enrichment was calculated as % of Input (ChIP/Input X 100). Enrichment fold in acetylation is calculated by normalizing the data against input DNA and by normalizing the enrichment with IgG antibody. Data represent the means \pm SEM of three wells. * p < 0.05, ** p < 0.01, *** p < 0.001, one-way ANOVA analysis. Data are representative of two independent experiments. The primers for ChIP-assay have been listed in Table S1.

ChIP-sequencing (ChIP-Seq) analysis

H3K27Ac-ChIP of murine CD8⁺ T cells treated with EnPGC-1 or DMSO vehicle were further sequenced to understand the genome-wide acetylation induced by EnPGC-1. ChIP-Sequencing was performed by Macrogen Inc. ChIP-Seq libraries were prepared using TruSeq DNA Sample Prep Kit following the protocol TruSeq ChIP Sample Preparation Guide, Part # 15023092 Rev. B. All libraries were sequenced to a depth of 100 million reads using the NovaSeq6000 sequencer to generate 151-bp paired-end library reads. Following the quality check, Trimmomatic, a fast, multithreaded command line tool was used to trim and crop Illumina (FASTQ) data as well as to remove adapters. Following the read trimming, a guided pipeline was used for the downstream analysis in the sequence e.g., Bowtie (read mapping), Picard (remove duplicates), MACS2 (peak calling) and ChIPseeker (peak annotation). Bowtie tool (version 1.1.2) was used to align short DNA sequences (reads) to the reference mouse genome (mm10). Further, MACS2 (version 2.2.2.20160309) captures the influence of genome complexity to evaluate the significance of enriched ChIP regions, and MACS improves the spatial resolution of binding sites through combining the information of both sequencing tag position and orientation. Duplicate reads were identified by Picard (version 0.118). Further, the final data were annotated using ChIPseeker tool (version v1.16.1). It supports annotating ChIP peaks and provides functions to visualize ChIP peaks coverage over chromosomes and profiles of peaks binding to TSS regions. FASTQ files are available through the Gene Expression Omnibus (GEO) accession number GSE175849.

RNA-seq data generation

Murine primary CD8⁺ T cells were TCR stimulated with anti-CD3/CD28 mAb and treated with PIPs for 48 h following the schedule mentioned in Figure 1B. Following the treatment, cells were harvested, and RNA was extracted using the Qiagen RNeasy kit from the treated groups. RNA integrity was assessed using a Bioanalyzer 2100 (Agilent Technologies) and deemed of good quality for conducting the RNA-Sequencing experiment. RNA-Sequencing was performed at Illumina platform by Macrogen Inc. RNA-Seq libraries were prepared using TruSeq Stranded mRNA LT Sample Prep Kit following the protocol TruSeq Stranded mRNA Sample Preparation Guide, Part # 15031047 Rev. E. All libraries were sequenced to a depth of 200 million reads using the NovaSeq6000 sequencer to generate 100-bp paired-end library reads. Mus musculus whole transcriptome sequencing was performed in order to examine the different gene expression profiles. Further, analysis was performed following the RNA-Seq data quality control, including filtering out low-quality reads, separating multiplexed samples by barcode, and removing 3'-adapter sequences, and provided resulting FASTQ files. The data were deposited at Gene Expression Omnibus (GEO) repository (<http://www.ncbi.nlm.nih.gov/geo>) and the FASTQ files are available through the GEO accession number GSE174750.

RNA-seq data analysis

To analyze the expression of Mus musculus CD8⁺ T cells, whole transcriptome, FASTQ files for each sample were mapped to reference genome mm10 with HISAT2. After the read mapping, Stringtie was used for transcript assembly. Expression profile was calculated for each sample and transcript/gene as read count, FPKM (Fragment per Kilobase of transcript per Million mapped reads) and TPM (Transcripts Per Kilobase Million). Performed read counting per gene and used gene count matrix for differential expression analysis with DESeq2. For differential expression analysis, known batches as "-1" and "-2" were included for samples sequenced at two different times using same schedule. Unknown batch variables were predicted with sva package and one variable was identified which was included as well. Gene-enrichment and functional annotation analysis was performed using Gene Ontology (www.geneontology.org/). The GO gene list have been listed in Table S2.

Measurement of OCR and ECAR using Seahorse XF analyzer

Oxygen consumption rate (OCR) and extracellular acidification rate (ECAR) were measured using an XFe96 Extracellular Flux analyzer (Seahorse Biosciences). Assay medium (OCR medium) was prepared as per recommendation (XF cell Mito Stress Test Kit, Seahorse Bioscience, 103015-100). Electron transport chain modulators e.g., Oligomycin (100 μ M), FCCP (100 μ M), and Rotenone/Antimycin A (50 μ M) were prepared in OCR media and were added 25 μ L of suspension in the wells (Oligomycin to well A; FCCP to B; Rotenone/Antimycin A to C and OCR buffer only well D) as per the manufacturer's recommendation. Calibration using calibrant buffer was done before measurement. 0.3 million cells per well were seeded in the XFe96 plate and the OCR/ECAR was measured. After the completion of run, different parameters were calculated from the OCR graph e.g. (a) basal respiration (measurement before oligomycin treatment – nonmitochondrial respiration) (b) ATP turnover (measurement before oligomycin - measurement after oligomycin treatment) (c) maximal respiration (measurement after FCCP treatment-non-mitochondrial respiration) (d) spare respiratory capacity is equal to subtraction of basal from maximal. The OCR medium contains glucose (10 mM) so we measured ECAR of the cells in same well as OCR. Basal ECAR should be considered the measurement immediately before oligomycin injection as the OCR media contains optimal glucose level. The double plot of OCR/ECAR for treated groups was plotted with the values of last measurement before oligomycin injection. Glycolytic capacity is the rate after the injection of oligomycin. Basal ECAR subtracted from glycolytic capacity gives the parameter known as glycolytic reserve. Related to [Figures 2B, 2C, 4H, 4I, S4C, and S4F](#).

QUANTIFICATION AND STATISTICAL ANALYSIS

Statistical analysis was performed using Prism 7. The variations of data were evaluated as the means \pm standard error of the mean (SEM). Subjects were chosen randomly from the pool with no blinding test for the treatment of subjects. Data represent the means \pm SEM of three wells (for all *in vitro* analysis). Data represent the means \pm SEM of five mice (In all the flow cytometry assays and measurements from *in vivo* experiment). For analyzing more than two variables, one-way ANOVA analysis followed by Sidak's multiple comparison test was performed while for comparing two groups, student t-test was performed. Data were considered as parametric and statistical tests were two-sided where data were considered significant with a p value <0.05 where the order of significant defined by *p < 0.05 , **p < 0.01 , ***p < 0.001 , ****p < 0.0001 . Data are representative of three independent experiments.

Supplemental information

**Targeted epigenetic induction
of mitochondrial biogenesis enhances
antitumor immunity in mouse model**

Madhu Malinee, Ganesh Namasivayam Pandian, and Hiroshi Sugiyama

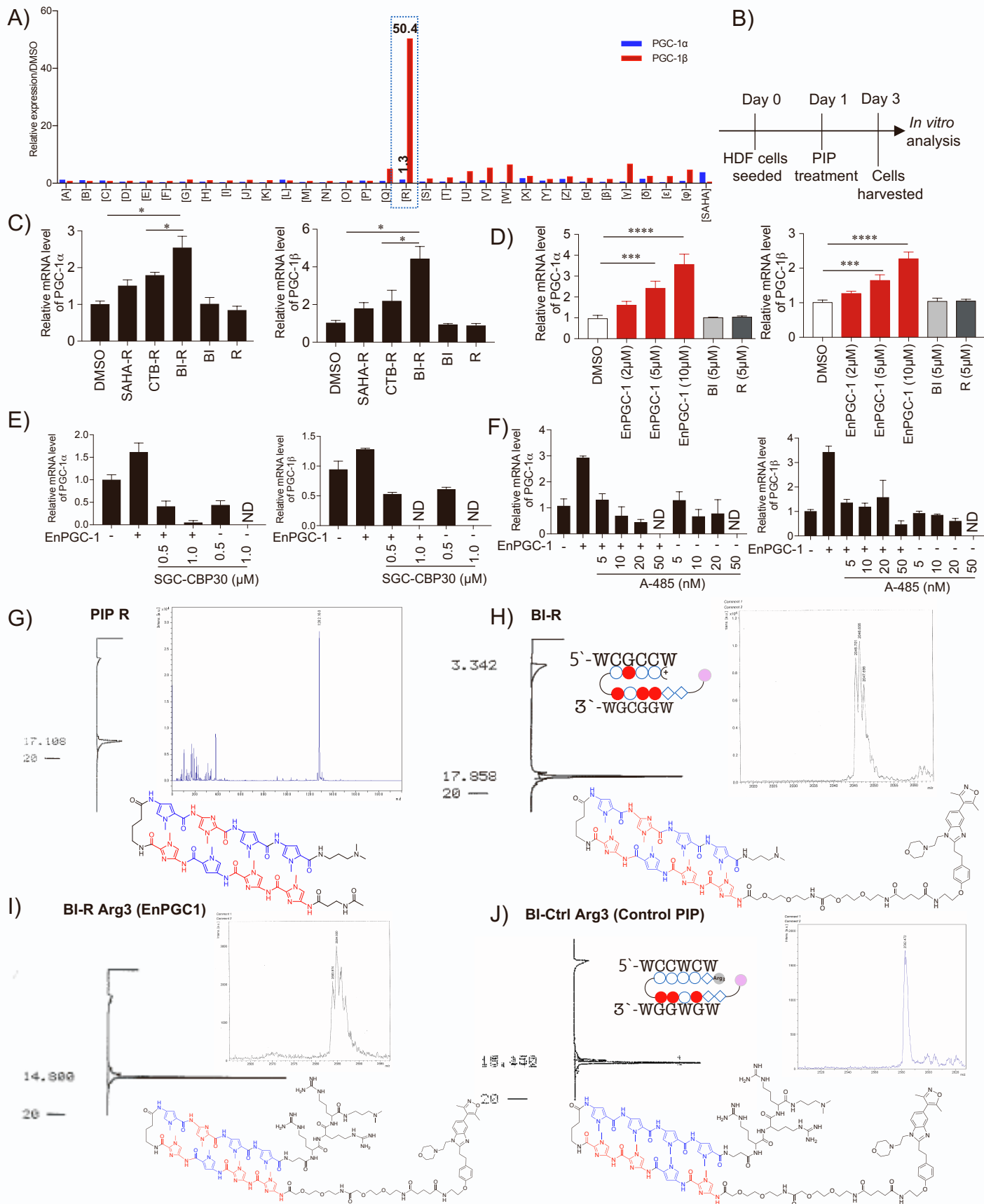


Figure S1. Sequence-specific PIP for PGC-1 α/β enhancement, related to Figure 1 and 2.

(A) Microarray data of HDF cells treated with SAHA-PIP library from our previous work were analyzed (Pandian et al., 2014b). Relative expression of PGC-1 α and PGC-1 β were plotted. (B) Schematic representation of experimental schedule of PIP treatment of HDF cells. (C) Transcript level of PGC-1 α (left) and PGC-1 β (right) in HDF cells on 3rd day post treatment (all PIPs were 5 μ M). (D) Transcript levels of PGC-1 α (left) and PGC-1 β (right) of the HDF cells treated with EnPGC-1 (2, 5, 10 μ M) and controls (BI and R, each 5 μ M conc.) (E, F) Transcript level of PGC-1 α and PGC-1 β of CD8⁺ T cells treated with EnPGC-1 along with a wide range of concentration of SGC-CBP30 (E) or A-485 (F). (G) Analytical HPLC t_R = 17.10 min; MALDI TOF MS m/z calcd for $C_{58}H_{72}N_{24}O_{11} + [M+H]^+$ 1281.3, Found: 1282.2, for PIP R. (H) Chemical architecture of PIP BI-R with 6-bp DNA recognition sequence (5'-WCGCCW-3'). Analytical HPLC t_R = 17.9 min; MALDI-TOF MS m/z calcd for $C_{98}H_{126}N_{30}O_{20} + [M+H]^+$ 2044.27, found 2045.70 for BI-R. (I) Analytical HPLC t_R = 14.80 min; MALDI-TOF MS m/z calcd for $C_{119}H_{167}N_{43}O_{24} + [M+H]^+$ 2583.92, found 2586.145 for BI-R Arg3(EnPGC1). (J) Chemical architecture of Control PIP with 6-bp DNA recognition sequence (5'-WCCWCW-3'). Analytical HPLC t_R = 15.4 min; MALDI-TOF MS m/z calcd for $C_{120}H_{168}N_{42}O_{24} + [M+H]^+$ 2582.93, found 2582.47 for BI-Ctrl Arg3 (Control PIP). (C-F) Data represent the means \pm SEM of three wells. * p < 0.05, ** p < 0.01, *** p < 0.001, **** p < 0.0001, one-way ANOVA analysis. Data are representative of three (C, D) or two (E, F) independent experiments.

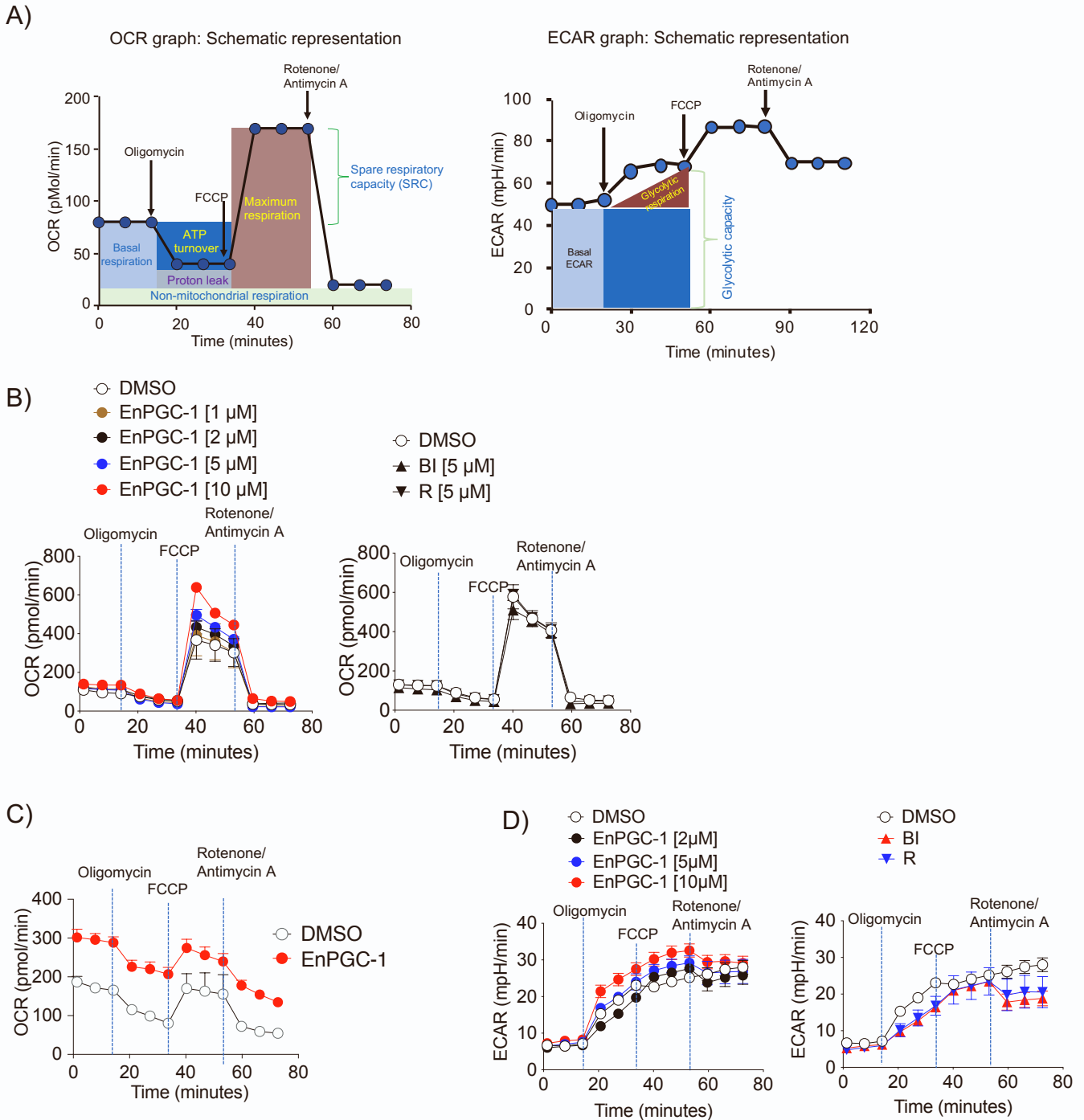


Figure S2. EnPGC-1-induced PGC-1 α/β enhancement results in increment in OCR, related to Figure 2.

(A) Schematic representations of OCR and ECAR graph are shown. OCR graph (left) shows addition of different ETC modulators and OCR associated parameters like basal respiration, maximal respiration, proton leak, non-mitochondrial respiration, ATP turnover and spare respiratory capacity. ECAR graph (right) shows basal ECAR, glycolytic respiration and glycolytic capacity. (B-C) OCR was measured for HDF cells (B) and iPS-induced cardiomyocytes (C) that were treated with PIPs using the treatment schedule shown in Supplemental Information S1B. (D) ECAR of *in vitro* PIP treated naïve CD8⁺ T cells from the experiment related with Figure 2B. (B-D) Data represent the means \pm SEM of three wells. Data are representative of three independent experiments.

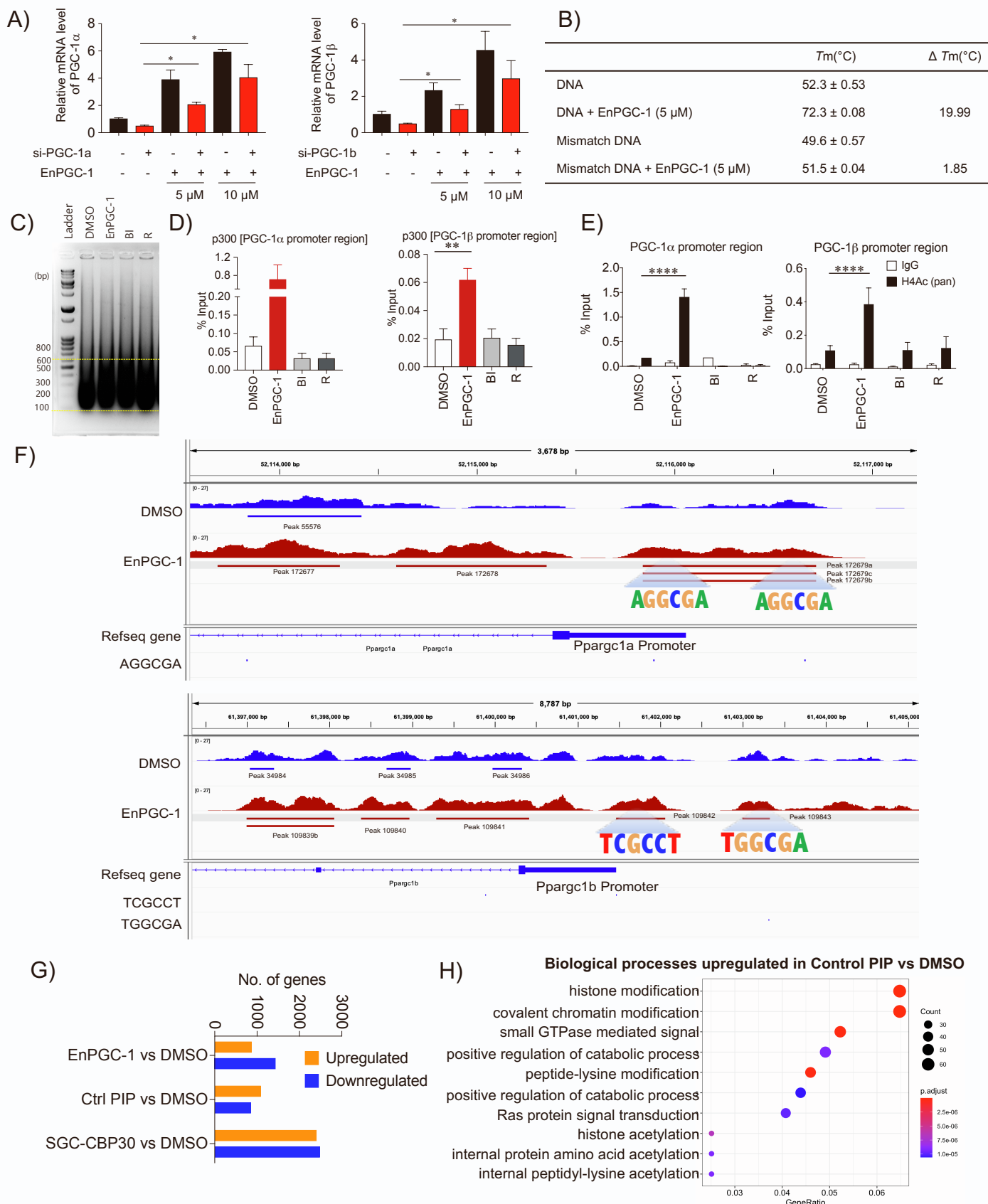


Figure S3. EnPGC-1 binding causes acetylation in promoter region of PGC-1 α/β and activate their expression, related to Figure 3.

(A) Transcript level of PGC-1 α (left) and PGC-1 β (right) from siRNA rescue experiment following the protocol shown in Figure 3A where EnPGC-1 was used dose-dependently. (B) The table shows the T_m and ΔT_m values of template DNA with or without EnPGC-1. Data represent the means \pm SEM of technical replicates. The given table is the representative of three independent experiments. (C-E) B16 murine melanoma cells were treated with PIPs (each 5 μM conc.) for 48 hours following the schedule mentioned in Supplemental Information S1B and ChIP assay was performed. (C) Agarose gel electrophoresis of fragmented DNA of B16 samples is shown. ChIP-PCR of p300 binding sequence (D) and histone H4-pan acetylation (E) in the promoter region of PGC-1 α (left) or PGC-1 β (right) is shown. (F) CHIP analysis of H3K27 acetylation in the promoter region of Ppargc1a (upper) and Ppargc1b (lower) are shown (related to Figure 3E). EnPGC-1 recognition sequences in the acetylated region are highlighted. (G) Number of differentially expressed genes is shown from RNA-seq analysis (related to Figure 3F-G). EnPGC-1 over DMSO shows differential expression of 2308 genes (871 upregulated; 1437 downregulated), Ctrl PIP over DMSO shows 1941 genes (1085 upregulated; 856 downregulated) while SGC-CBP30 over DMSO shows 4886 genes that were differentially expressed (2402 upregulated; 1484 downregulated). (H) Biological processes upregulated genes in Control PIP over DMSO is shown for RNA-seq analysis (related with Figure 3F). (A, D-E) Data represent the means \pm SEM of three wells. * $p < 0.05$, ** $p < 0.01$, *** $p < 0.001$, **** $p < 0.0001$, one-way ANOVA analysis. Data are representative of three independent experiments.

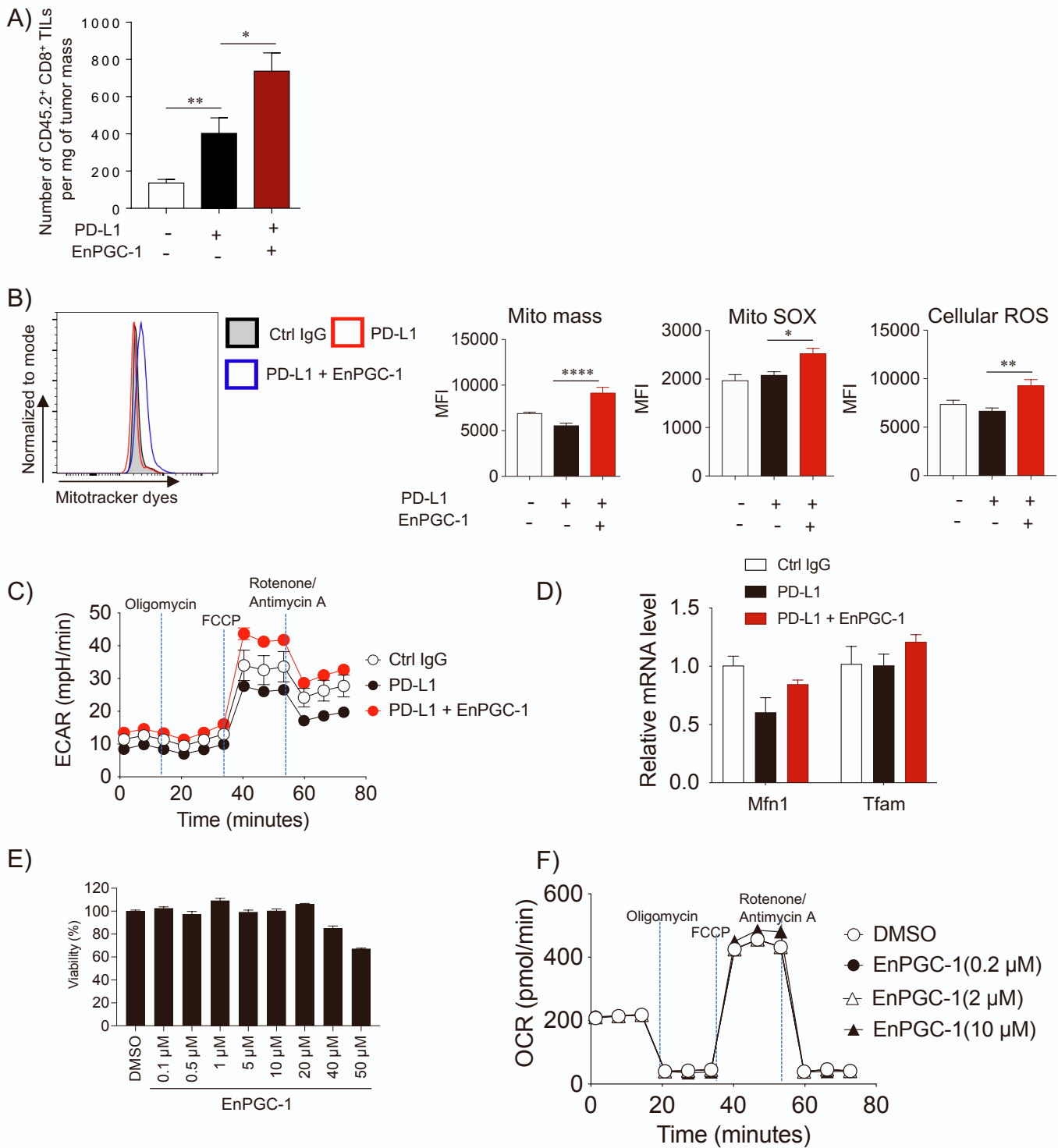


Figure S4. EnPGC-1 treatment synergize with PD-1 blockade *in vivo*, related to Figure 4.

(A) Absolute number of CD45.2⁺ CD8⁺ T cells in the tumor mass from respective group of *in vivo* analysis (related with Figure 4A, D-L). (B) DLN cells from Figure 4D, were stained with anti-CD8, and mitochondrial dyes. DLN CD8⁺ T cells are further gated on to assess mitochondrial dye staining. Representative histogram of mitochondrial dye staining is shown (left). MFI of different dyes were calculated and compared among *in vivo* experimental treated groups (right). (C) ECAR of purified DLN CD8⁺ T cells were measured in the same wells along with OCR measurement shown in Figure 4H. (D) Transcript level of indicated genes related to Figure 4L. (E) Cytotoxicity assay was performed for EnPGC-1 on MC38 cells. MC38 tumor cells were seeded and next day treated with different indicated concentration of EnPGC-1. After 48 hours of treatment viability was assessed using WST-8 kit. (F) OCR of MC38 cells treated with EnPGC-1 dose-dependently following the experimental schedule shown in Supplemental Information S1B. (A, B) Data represent the means \pm SEM of 5 mice. * $p < 0.05$, ** $p < 0.01$, one-way ANOVA analysis. (C-F) Data represent the means \pm SEM of three wells. Data are representative of three independent experiments.

Table S1. List of primers used for qRT-PCR and STAR Methods, related to Figure 1, 2, 3, and 4.

Transcript	Forward primer	Reverse primer
qCR primers for human gene transcript		
PGC-1 α	TGGAGTGACATAGAGTGTGCTGC	CTCAAATATGTTTCGAGGCTCA
PGC-1 β	GCTCTTCCAGATTGACAGTGAGA	GTAGCAGTGAAAGCTCGTCCA
GAPDH	GACGCTGGGGCTGGCATTG	GCTGGTGGTCCAGGGGTC
qPCR primers for murine gene transcript		
PGC-1 α	AAACTTGCTAGCGGTCTCTCA	TGGCTGGTGCCAGTAAGAG
PGC-1 β	GGTGTTCCGGTGAGATTGTAGAG	GTGATAAAACCGTGCTTCTGG
GAPDH	CATCACTGCCACCCAGAAGACTG	ATGCCAGTGAGCTTCCCCTTCAG
LCAD	GGTGAAAACGGAATGAAAGG	GGCAATCGGACATCTTCAAAG
MCAD	TGTTAATCGGTGAAGGAGCAG	CTATCCAGGGCATACTTCGTG
Cpt1a	CCATCCTGTCCTGACAAGGTTTAG	CCTCACTTCTGTTACAGCTAGCAC
ATP5A1	CATTGGTGATGGTATTGCGC	TCCCAAACACGACAACCTCC
Bcl2	GGACTTGAAGTGCCATTG GT	AGCCCCCTCTGTGACAGCTTA
BIRC3	ACGCAGCAATCGTGCAATTTTG	CCTATAACGAGGTCACTGACG
UQCRC1	ACGGTGGGAGTGTGGATTGAC	CATTGCCAGGCCGATTCTTTG
MFN1	CCAGGTACAGATGCACCACAG	TTGGAGAGCCGCTCATTACCT
NRF2	TGAAGTTCGCATTTTGATGGC	CTTTGGCTCTGGCATCTCTAC
TFAM	CACCCAGATGCAAAACTTTTCAG	CTGCTCTTTATACTTGCTCACAG
ChIP qPCR primers for murine gene promoter		
PGC-1 α Promoter	GCGTTACTTCACTGAGGCAGAG	CACACAGCACACACTCATGCAG
PGC-1 β Promoter	GGAGCAGGAAAAGCCGGGG	CGTTCCCCGCCATCTTCC
mtDNA copy assessment in murine cells		
ND1	CTAGCAGAAACAAACCGGGC	CCGGCTGCGTATTCTACGTT
HK2	GCCAGCCTCTCCTGATTTTAGTGT	GGAACACAAAAGACCTCTTCTGG
siRNA sequence		
siPGC-1 α	CACAACUCCUCCUCAUAAAAdTdT	
siPGC-1 β	CUCAUUCGCUACAUGCAUAdTdT	
siCtrl	CAAUACUCUACAAACCCUCdTdT	
Tm assay DNA template		
EnPGC1-DNA	5'-GGCACGCCTCGG-3'	
Mismatch-DNA	5'-GGCAGACGTCGG-3'	